

Multi-Wavelength Observations of the Spatio-Temporal Evolution of Solar Flares with AIA/SDO: I. Universal Scaling Laws of Space and Time Parameters

Markus J. Aschwanden

Lockheed Martin Advanced Technology Center, Org. ADBS, Bldg.252, 3251 Hanover St., Palo Alto, CA 94304, USA; e-mail: aschwanden@lmsal.com

and

Jie Zhang and Kai Liu

School of Physics, Astronomy and Computational Sciences, George Mason University, 4400 University Dr., MSN 6A2, Fairfax, VA 22030, USA; e-mail: jzhang7@gmu.edu

ABSTRACT

We extend a previous statistical solar flare study of 155 GOES M- and X-class flares observed with AIA/SDO (Aschwanden 2012) to all 7 coronal wavelengths (94, 131, 171, 193, 211, 304, 335 Å) to test the wavelength-dependence of scaling laws and statistical distributions. Except for the 171 and 193 Å wavelengths, which are affected by EUV dimming caused by coronal mass ejections (CMEs), we find near-identical size distributions of geometric (lengths L , flare areas A , volumes V , fractal dimension D_2), temporal (flare durations T), and spatio-temporal parameters (diffusion coefficient κ , spreading exponent β , and maximum expansion velocities v_{max}) in different wavelengths, which are consistent with the universal predictions of the fractal-diffusive avalanche model of a slowly-driven self-organized criticality (FD-SOC) system, i.e., $N(L) \propto L^{-3}$, $N(A) \propto A^{-2}$, $N(V) \propto V^{-5/3}$, $N(T) \propto T^{-2}$, $D_2 = 3/2$, for a Euclidean dimension $d = 3$. Empirically we find also a new strong correlation $\kappa \propto L^{0.94 \pm 0.01}$ and the 3-parameter scaling law $L \propto \kappa T^{0.1}$, which is more consistent with the logistic-growth model than with classical diffusion. The findings suggest long-range correlation lengths in the FD-SOC system that operate in the vicinity of a critical state, which could be used for predictions of individual extreme events. We find also that eruptive flares (with accompanying CMEs), have larger volumes V , longer flare durations T , higher EUV and soft X-ray fluxes, and somewhat larger diffusion coefficients κ than confined flares (without CMEs).

Subject headings: Sun: Solar Flares — Statistics — magnetic fields

1. INTRODUCTION

Space and time scales are the most fundamental parameters in any physical system. Correlations and scaling laws between spatial and temporal parameters reveal the characteristics of various physical transport processes, such as motion in gravitational or electromagnetic fields, random walk processes, diffusion, conduction, turbulence, percolation, branching theory, network systems, etc. Here we focus on transport processes in solar flares, which to the best of our knowledge, are governed by magneto-hydrodynamic (MHD) processes and kinetic particle physics in coronal plasmas. However, kinetic theory and non-ideal MHD involve microscopic processes that exhibit a high level of complexity due to the large number of degrees of freedom, which is difficult or impossible to characterize with macroscopic quantities.

A relatively new method to understand the complexity of nonlinear energy dissipation processes is the concept of *self-organized criticality (SOC)*, pioneered by Bak et al. (1987; 1988), applied to solar flares by Lu and Hamilton (1991), and reviewed in a number of recent textbooks (Aschwanden 2011, 2013; Pruessner 2012). SOC can be considered as a basic physical mechanism, universally occurring in systems with many coupled degrees of freedom in the limit of infinitesimal external forcing. Such nonlinear systems are driven in the vicinity of a critical state, which is maintained by a self-organizing feedback mechanism in a robust manner that does not need any fine-tuning of physical parameters. The macroscopic evolution of an instability in a SOC system, triggered by a random disturbance that exceeds the local threshold of the instability, is governed by nearest-neighbor interactions on a microscopic level, which emerge and evolve over macroscopic scales in spatial volumes that exhibit long-range correlation lengths. These long-range correlation lengths demarcate zones with coherent deviations from the critical state, and thus indicate that nature self-organizes to the *vicinity of a critical state*, rather than being exactly at the edge of a critical state, which can be probed with correlation functions $C(\mathbf{r}, t)$ (Jensen 1988, Section 2.4),

$$C(\mathbf{r}, t) = \langle B(\mathbf{r}_0, t_0)B(\mathbf{r}_0 + \mathbf{r}, t_0 + t) \rangle_{\mathbf{r}_0, t_0} - \langle B(\mathbf{r}_0, t_0) \rangle^2, \quad (1)$$

where $B(\mathbf{r}, t)$ is a physical observable in a SOC system, such as, for instance, the non-potential magnetic field component in the solar corona. Nonlinear energy dissipation events in SOC systems, also called *avalanches* in SOC jargon, thus evolve over macroscopic length scales L that show some degree of correlation, such as zones with stressed or twisted magnetic fields (that are misaligned by some angle to the potential field), along which avalanches can propagate and evolve. The spatial scales of solar flares thus convey information that is equivalent to the correlations length. The correlation length can reveal macroscopic zones with coherent deviations from criticality and can be used to predict event sizes. For instance, free energy computed from the non-potential magnetic field near the neutral line is used to forecast flares, coronal mass ejections (CMEs), and filament eruptions (e.g., Schrijver 2007, Falconer et al. 2011, 2012). Statistics of spatial scales L of solar flares, which can be expressed as *probability distribution functions (PDFs)* or *occurrence frequency distributions* $N(L)$, exhibit ubiquitous powerlaw functions that are the hallmark of SOC systems. Since SOC systems evolve into the vicinity of a critical state, where long-range correlation lengths exist (Jensen 1988, Section 2.4), small disturbances can trigger small or large avalanches, which do not depend on any particular physical mechanism, such as, for instance, magnetic reconnection processes that produce solar flares.

In this study we investigate the universal behavior of spatial and temporal scales in solar flares, which are related to each other in terms of a classical (or an anomalous) diffusion process, governed by the statistics of a random walk process (Aschwanden 2012b). We show that the statistical distributions and correlations of spatial and temporal scales in solar flares are independent of other physical parameters. In contrast, other observables, such as photon fluxes do depend on physical parameters and are not universal for SOC processes. In solar (and astrophysical) observations, photon fluxes are observed at various wavelengths, which depend on physical parameters such as the electron temperature, density, or pressure, and thus scaling laws, correlations, and size distributions of observed photon fluxes are wavelength-dependent, and not universal, which will be modeled in Paper II.

2. THEORETICAL DEFINITIONS

The basic theory to interpret our statistical measurements of solar flare parameters is the *fractal-diffusive avalanche model of slowly-driven self-organized criticality systems (FD-SOC)*, described and tested with cellular automaton simulations in Aschwanden (2012a), and applied to solar flares in Aschwanden (2012b).

This theoretical model consists of four components: (1) scaling laws of Euclidean spatial parameters (in terms of the scale-free probability conjecture, Section 2.1); (2) the fractal geometry of the internal structure of SOC avalanches (Section 2.2); (3) the spatio-temporal evolution of SOC avalanches (in terms of fractal-diffusive transport, Section 2.3); and (4) physical scaling laws between observables and geometric SOC parameters (such as the flux-volume relationship; Paper II). The first three parts have universal validity in the sense that they can be derived from physics-free, pure mathematical and statistical probabilities, while the fourth component depends on the specific physical mechanism that controls the dynamics of a SOC avalanche and thus the observables. In this study we involve multi-wavelength observations of solar flares, which may exhibit different scaling laws depending on the wavelengths, according to the involved physical mechanism. In this Paper I we analyze spatial and temporal parameters, which can be described by universal scaling laws that govern the first three components of our FD-SOC model, while we derive and test the scaling laws that concern the physics-based (fourth) component of the FD-SOC model in Paper II.

2.1. The Scale-Free Probability Conjecture

Typically, probability distribution functions (PDF) like Gaussian, binomial, Poisson, exponential, or powerlaw functions are adopted to describe likelihoods for counting or flux measurement scenarios. Most probability distributions in *self-organized criticality* (SOC) systems, which produce nonlinear dissipation events (also called *avalanches*), exhibit powerlaw functions over some parameter range of length scales and time scales. Our approach to understand the powerlaw nature of SOC systems is the so-called *scale-free probability conjecture*, which is based purely on a statistical argument, in analogy to Gaussian distributions that can be derived from binomial statistics.

In SOC models (Bak et al. 1987), which produce avalanches in a multiplicative manner over some time interval of coherent growth, the statistics is fundamentally different from the random additivity of incoherent processes with Gaussian statistics. The classical SOC paradigm is a sandpile with a critical slope that is self-adjusting (or self-organizing) after each avalanche. However, the local slopes are not exactly at the critical threshold, but show some small irregular deviations, which are called *coarse-granularity* or *micro-roughness*. These deviations in the vicinity of the critical threshold have spatial long-range correlation lengths that enable chain reactions over large distances once a local instability sets in. Thus, a SOC system has the ability to produce avalanches over a large range of sizes S , which sometimes exceeds several orders of magnitude. We argue that the statistical probability distribution function of an avalanche with length scale L in any Euclidean space with dimension d^1 ($d = 1, 2, 3$), is (Aschwanden 2012a),

$$N(L) \propto L^{-d}, \quad (2)$$

which represents a powerlaw distribution function. This simple statistical probability argument is independent of the physical process that drives a SOC avalanche, such as gravity in the case of sandpiles or magnetic reconnection in the case of solar flares, and thus has universal validity for SOC systems.

Other size distributions of geometric or spatial parameters that can directly be derived from Eq. (2) are the Euclidean 2-D avalanche area A and the 3-D avalanche volume V . If we simply define the Euclidean area A in terms of the squared length scale, i.e., $A \propto L^2$, we obtain the area size distribution $N(A)$ by

¹In the previous study we used the notation $S = 1, 2, 3$ for the Euclidean spatial dimension (Aschwanden 2012a), but rename it here to $d = 1, 2, 3$, to be more consistent with literature and to avoid confusion with the parameter S that is generally used to characterize the size of a SOC avalanche (e.g., Bak et al. 1987; Pruessner 2012).

substitution,

$$N(A)dA \propto N[L(A)] \left| \frac{dL}{dA} \right| dA \propto A^{-(1+d)/2} dA , \quad (3)$$

yielding $N(A) \propto A^{-2}$ for 3-D phenomena ($d = 3$).

Similarly we define the Euclidean volume, i.e., $V \propto L^d$, which can be substituted to obtain the volume size distribution $N(V)$,

$$N(V)dV \propto N[L(V)] \left| \frac{dL}{dV} \right| dV \propto V^{-(1+2/d)} dV , \quad (4)$$

yielding $N(V) \propto V^{-5/3}$ for 3-D phenomena ($d = 3$).

Thus, we have universal predictions for the size distributions of length scales, areas, and volumes of SOC avalanches that depend only on the Euclidean space dimension d , which will be tested in Section 3 with multi-wavelength images of solar flares.

2.2. Fractal Geometry

The complex topology of a SOC avalanche at a given instant of time can be described by a fractal dimension (Bak and Chen 1989), for instance with the Hausdorff dimension D_d (in Euclidean space dimension $d = 1, 2, 3$),

$$V_d = L^{D_d} . \quad (5)$$

An example of several time instances t of a SOC avalanche with determination of the Hausdorff dimension $D_d(t)$ as a function of time is shown in Figs. 2 and 3 of Aschwanden (2012a). The mean value of the minimum $D_{d,min} \approx 1$ and maximum dimension $D_{d,max} \lesssim d$ is a good approximation of the average fractal dimension D_d of an avalanche, for each Euclidean dimension $d = 1, 2, 3$, i.e.,

$$D_d \approx \frac{D_{d,min} + D_{d,max}}{2} = \frac{1 + d}{2} . \quad (6)$$

So, we expect an average fractal dimension of $D_3 = 2.0$ for 3-D avalanches.

2.3. Fractal Diffusion in SOC Systems

The third component of the FD-SOC model concerns the spatio-temporal evolution of SOC avalanches, which can be characterized by the generalized relationship for diffusion (Aschwanden 2012a),

$$r(t) = \kappa(t - t_k)^{\beta/2} , \quad (7)$$

where $r(t)$ represents the evolution of the flare radius $r(t)$, t_k the start time of the diffusion process, κ is the diffusion coefficient, and β is the diffusion (or spreading) powerlaw exponent. The case of $\beta = 1$ corresponds to classical diffusion or random walk, while the regimes of $0 < \beta < 1$ corresponds to sub-diffusion, and $1 < \beta < 2$ to super-diffusion or hyper-diffusion (also called Lévy flights by Mandelbrot), both representing anomalous diffusion processes. The lower limit of the diffusion powerlaw exponent $\beta = 0$ can be identified with a logistic growth process (Aschwanden 2012a), while the upper limit of $\beta = 2$ corresponds to linear growth. Values of $\beta > 2$ would indicate nonlinear growth characteristics. The various evolutions are pictured in Fig. 1.

Since most instabilities, including SOC avalanches, start with an exponential growth phase, and saturate at a maximum level, it is useful to describe the evolutionary time profile with a *logistic equation*. The combined evolution of a logistic growth phase and a diffusive saturation phase can be analytically expressed with a smooth transition inbetween (Aschwanden 2012b; Section 2.5),

$$r(t) = \begin{cases} r_\infty \left[1 + \exp\left(-\frac{t-t_1}{\tau_G}\right) \right]^{-1/3} & \text{for } t \leq t_1 \\ \kappa(t-t_k)^{\beta/2} & \text{for } t > t_1 \end{cases} \quad (8)$$

where r_∞ represents the final spatial scale of $r(t)$ in the case of strict logistic growth ($\beta = 0$), and τ_G represents the e-folding growth time. The time evolution $r(t)$ is shown in Fig. 1 for five different diffusion exponents ($\beta=0.0, 0.5, 1.0, 1.5, 2.0$). We will fit this analytical evolutionary function (Eq. 8) to the flare radius evolution $r_{\lambda,th}(t)$ for different wavelengths λ and flux thresholds q_{th} in Section 3, in order to obtain statistics on the diffusion coefficients κ and diffusion exponents β .

If the diffusion coefficient κ is uncorrelated with the flare radius $L = r(t = t_{end})$ or flare duration $T = (t_{end} - t_{start})$, we expect (according to Eq. 7 for $T = [t - t_k]$) a scaling law between the spatial L and time scale T ,

$$L \propto T^{\beta/2}, \quad (9)$$

which constitutes another universal scaling law, being dictated by the statistical nature of a diffusion process, such as random walk statistics in the case of classical diffusion ($\beta = 1$).

Combining the scale-free probability distribution of length scales, $N(L) \propto L^{-d}$ (Eq. 2), with the universal scaling law for time scales, $L \propto T^{\beta/2}$ (Eq. 9), we can then directly predict the probability distribution of time scales, $N(T)$,

$$N(T)dT = N(L[T]) \left| \frac{dL}{dT} \right| dT \propto T^{-[1+(d-1)\beta/2]} dT, \quad (10)$$

which for 3-D phenomena ($d = 3$) predicts a powerlaw slope of $\alpha_T = 1 + \beta$. Thus, the powerlaw slope for time durations will be $\alpha_T = 2.0$ for classical diffusion ($\beta = 1$), or lay in the range of $\alpha_T = 1, \dots, 2$ for sub-diffusion, or in the range of $\alpha_T = 2, \dots, 3$ for hyper-diffusion.

In conclusion, according to the FD-SOC model, the probability distributions of space L and time scales T depend only on the Euclidean space dimension d and diffusion exponent β . The internal fractal geometry of a SOC avalanche is quantified by the fractal dimension $D_d \approx (1 + d)/2$ and has a universal characteristics also. In contrast, the probability distributions of other observable parameters, such as the flux F_λ observed in a given instrumental wavelength λ , do depend on specific physical mechanisms observed in SOC avalanches, which can be quantified in terms of a flux-volume scaling law, $F_\lambda \propto V^\gamma$, the fourth component of the FD-SOC model, which we will explore in Paper II.

3. OBSERVATIONS, DATA ANALYSIS, AND RESULTS

The observations and the data analysis method are similar to the previous study of Aschwanden (2012b). The two major differences to the previous study are that (i) we analyze a multi-wavelength data set that includes all seven coronal filters (94, 131, 171, 193, 211, 304, 335 Å) of AIA/SDO (Lemen et al. 2012; Boerner et al. 2012), compared with the earlier single-wavelength study (335 Å), and (ii) we are using five relative flux thresholds for the identification of flare areas, while the previous study used only two fixed flux threshold levels. The main motivation for this extended study is that we want to distinguish universal

(statistical) from wavelength-dependent (physical) scaling laws, as well as to explore possible systematic uncertainties in the flare area definition. In the following subsections we discuss a number of systematic uncertainties (such as the effects of flux thresholds in the flare area measurements, possible dependencies of flux size distributions on the observed wavelengths, the effects of flux saturation in flare area measurements from overexposed images, effects of coronal dimming, and uncertainties in the definition of flare durations). Random errors due to small-number statistics and the corresponding accuracy of powerlaw fits are discussed in Section 7.1.7 of Aschwanden (2011). We determined also formal errors of powerlaw fits, but do not list them here, because larger uncertainties occur due to the deviations from ideal powerlaws, the choice of the lower cutoffs (where incomplete sampling applies) and upper cutoffs (for the rare largest events). Instead we list empirical uncertainties of the powerlaw slopes in terms of the means and standard deviations obtained from averaging the slopes among different wavelengths (bottom lines in Tables 1-6) and among different flux thresholds (last columns in Tables 1-6).

3.1. Observations

The dataset consists of 155 solar flares that includes all M- and X-class flares detected with AIA/SDO during the first two years of the SDO mission (during the time interval of 2010 May 13 and 2012 March 31). All AIA images have a cadence of $\Delta t = 12$ s and a pixel size of $\Delta x = 0.6'' \approx 435$ km, which corresponds to a spatial resolution of $2.5\Delta x = 1.5'' \approx 1100$ km. We analyzed about 100 time frames for each flare in 7 wavelengths, which amounts to a total number of $\approx 10^5$ images or ≈ 2 Terabytes of AIA data.

The data analysis for a single wavelength is described in some detail in Section 3.2 of Aschwanden (2012b), where two fixed flux thresholds were used at $F_{335,th} \geq 100$ and ≥ 200 DN s⁻¹. Here we use five different flux thresholds $F_{\lambda,th}$ in each of the seven wavelengths, which were set at $q_{th} = F_{\lambda,th}/F_{\lambda,max} = 0.01, 0.02, 0.05, 0.1,$ and 0.2 of the peak flux $F_{\lambda,max}$ during the flare time interval. The use of multiple thresholds yields more robust normalized flare areas, because fuzzy fine structures of the flare boundaries are better averaged out at different flux levels (see Section 3.2 and Figure 3a). Two flare area definitions are used: (i) The instantaneous flare area $a_{\lambda,th}(t)$ that entails all pixels with a flux above the flux threshold at time t , and (ii) the time-integrated flare area $A_{\lambda,th}(< t)$ that combines pixels that had a flux exceeding the threshold anytime during the flare time interval $[t_{start}, t]$. We will see that the instantaneous flare area a has a fractal characteristics, while the time-integrated flare area A has a near Euclidean, space-filling topology. Defining an equivalent circular area, we can then characterize a length scale $r_{\lambda,th}$ that corresponds to the radius of this circular area,

$$r_{\lambda,th} = \sqrt{A_{\lambda,th}/\pi}. \quad (11)$$

An example of the analysis of one flare event (#28) in one single filter (193 Å) is shown in Fig. 2, showing the flux profiles $F_{193}(t)$ and flare radius profiles $r_{193,th}(t)$ for the 5 different thresholds. This figure can be compared with Fig. 2 in Aschwanden (2012b), where the same event is analyzed in a different wavelength (335 Å) with two different thresholds. The 193 Å images shown in Fig. 2 exhibit also episodes of flux saturation due to too long exposure times, which however, are adjusted in subsequent images with the automated exposure control mechanism of AIA. The flux saturation can lead to significant underestimates of the peak flux (measured in a single pixel), but the missing flux in saturated flare areas represents a small fraction of the total image-integrated EUV flux and inferred flare area here, as the continuity of the total flux profiles $F_{193}(t)$ and flare radius profiles $r_{193,th}(t)$ show in Fig. 2.

The 7 temperature filters of AIA are sensitive to coronal plasma in the temperature range of $\log(T) \approx$

5.2 – 7.7 (Boerner et al. 2012). We will describe the thermal response functions of these wavelength filters in Paper II, where we perform a differential emission measure (DEM) analysis and determine wavelength-independent physical parameters, such as electron densities and electron temperatures.

3.2. Normalization of Threshold-Dependent Length Scale

Since we measure the length scale $L_{\lambda,th}$ from the flare area $A = \pi r_{\lambda,th}^2$ at five different flux threshold levels $q_{th} = 0.01, 0.02, 0.05, 0.1, 0.2$ of the maximum flux $F_{\lambda,max}$, we obtain flare areas and length scales of different sizes $L_{\lambda,th}$, where the lowest flux threshold level of $q_{th} = 0.01$ encompasses the largest flare areas, while the highest flux threshold level of $q_{th} = 0.2$ encloses the smallest flare areas, among the different threshold levels. In order to eliminate this dependence of the length scale on the flux threshold, we normalize all flare areas to a fixed threshold level of $q_{th} = 0.05$. We find empirically the following relationship between the length scales $L(q_{th})$ measured at a threshold level q_{th} and a normalized length scale $L^{norm} = L(0.05)$ defined at a fixed threshold level of $q_{th} = 0.05$ (Fig. 3, top panel),

$$L_{\lambda}(q_{th}) = L_{\lambda}(0.05) \left(\frac{q_{th}}{0.05} \right)^{-0.383}. \quad (12)$$

This relationship works equally well for all 7 wavelengths, as demonstrated with the scatterplot shown in Fig. 3 (bottom panel) between the measured length scales $L_{\lambda}(q_{th})$ and the normalized length scales $L_{\lambda}(0.05)(q_{th}/0.05)^{-0.383}$. This relationship quantifies that the ratio $L_{\lambda}(q_{th})/L_{\lambda}(0.05)$ of the measured length scales are factors of 1.85, 1.42, 1.00, 0.77, and 0.59 different at the various thresholds $q_{th} = 0.01, 0.02, 0.05, 0.1, 0.2$ with respect to a chosen fixed threshold of $q_{th} = 0.05$. These scale factors can be seen in the vertical scale of the fitted flare expansion curves $r_{\lambda,th}$ in the example shown in Fig. 2 (middle panel). The normalized flare areas synthesized from five different thresholds average the fuzzy contours of flare areas better than the area obtained from a single arbitrary flux threshold. We apply this threshold normalization (Eq. 12) to all parameters that are derived from a measured length scale L , such as to the flare area A , the flare volume V , the diffusion coefficient κ , and the maximum velocity v_{max} .

In principle, the normalization of length scales represents a multi-variate problem, but the excellent correlation of the length scale with the flux threshold (Eq. 12 and Fig. 3, top panel) justifies a simplified bivariate treatment.

3.3. Statistics of Flare Areas

The flare area A is the most directly measured quantity among the geometric parameters, while the length scale L and volume V are deduced from the area A . From the 155 flares we derived a flare area $A_{\lambda,th}(t = t_{end})$ at the end time t_{end} of each flare, for each of the 7 wavelengths λ and 5 flux thresholds q_{th} . The end time t_{end} of a flare is defined (according to NOAA flare catalogs) when the GOES 1-8 Å flux decays to the half value of the (preflare background-subtracted) peak flux (marked with a vertical dashed line near the right border of the panels shown in Fig. 2). Histogramming the observed flare areas A , we find flare areas between $A_{min} = 44 \text{ Mm}^2$ and $A_{max} = 19,000 \text{ Mm}^2$. All powerlaw fits in 7 wavelengths λ and 5 thresholds q_{th} are shown separately in Fig. 4. Since the log-log histograms of flare areas extend over about two decades for each subset, the powerlaw slopes can be determined somewhat more accurately ($\approx 15\%$) than for length scales. The values for each wavelength and threshold are listed in Table 2. The overall average is, where the error bar represents the standard deviation from averaging the area parameter from different wavelengths

and flux thresholds (see Table 2),

$$\begin{aligned} \alpha_A &= 2.1 \pm 0.3 && \text{Observations} \\ \alpha_A &= 2 && \text{Theory (for } d = 3) \end{aligned} \tag{13}$$

which also agrees with the predicted value $\alpha_A = 2$ for SOC phenomena in 3-D space (Eq. (3); for $d=3$). Similarly as for length scales, we find for flare areas no wavelength dependence (Figs. 5b and 6b). There is only a very slight trend that the flare area depends on the flux threshold (Fig. 7b and Table 2).

Inspecting the wavelength dependence of the powerlaw distributions in detail (Fig. 4), we do find the largest deviations from predicted powerlaws for the wavelengths of 171 and 193 Å at low threshold levels of $q_{th} = 0.01 - 0.02$. Watching the flare movies it is obvious that the EUV dimming caused by coronal mass ejections is best visible in the 171 and 193 Å channels, because they are most sensitive to the bulk of the ejected plasma at an electron temperature of $T_e \approx 1 - 2$ MK plasma. The ejected plasma causes a dimming in the EUV flux (due to the proportionality between coronal mass column depth and optically thin emission) in such a way that the bright flare area is substantially reduced and underestimated, compared with the other unimpeded wavelengths. Thus, it is recommendable to exclude those two EUV filters for this type of statistical studies of spatio-temporal flare parameters. Inquiring the standard deviations for each wavelength range in Table 2, we find that the wavelengths of 94, 131, 304, and 335 Å have the smallest variation of the powerlaw slope α_A averaged over different flux thresholds, and thus are all equally suitable for statistical studies.

Foreshortening effects as a function of the center-to-limb distance could introduce a cosine-dependence if the flare volumes would be 2-dimensional (as seen in H- α or white light), but observational measurements in EUV and soft X-rays, and volume models in terms of flare loop arcades, yield a much weaker effect that is probably not measurable due to random variations of the flare area geometry, orientation, and filling factors (Aschwanden and Aschwanden 2008a,b).

3.4. Statistics of Length Scales

We histogrammed the length scales $L_{\lambda,th}$ (derived from the flare area $A_{\lambda,th}$ according to Eq. (11)) and fitted a powerlaw function in the upper half of the logarithmic size range (similarly as shown for flare areas in Fig. 4). The range of length scales extends from $L_{min} = 3.7$ Mm to $L_{max} = 78$ Mm for different wavelengths (normalized to a common flux threshold of $q_{th} = 0.05$), so it does cover slightly more than one logarithmic decade. Since the lower half of this logarithmic length distribution shows a rollover due to undersampling of length scales near the flux threshold (of M1 GOES class flares) in the selection of events, we can fit only a range of length scales that extends over about a half decade, leading to uncertainties of $\approx 20\%$ in the determination of the powerlaw slope. We tabulate the obtained powerlaw slopes α_L of length scales in Table 1, and average them in each wavelength and flux threshold separately. The overall average and standard deviation of all 7×5 powerlaw fits is (see also Table 1),

$$\begin{aligned} \alpha_L &= 3.2 \pm 0.7 && \text{Observations} \\ \alpha_L &= 3 && \text{Theory (for } d = 3) , \end{aligned} \tag{14}$$

which agrees well with the predicted value $\alpha_L = 3$ for SOC phenomena in 3-D space (Eq.(2); for $d=3$).

Another important result is that we see no dependence on the wavelength, as the powerlaw fits of the size distributions in Fig. 5a show, or the powerlaw slopes α_L as a function of the wavelength λ shown in

Fig. 6a, and listed in Table 1, which supports our assumption of universality for the length scale distribution $N(L)$. However, there is a slight trend that the powerlaw slope flattens with increasing flux threshold, from $\alpha_L = 4.0 \pm 0.7$ at the 1% threshold level to $\alpha_L = 2.8 \pm 0.3$ at the 20% threshold level (Fig. 7a and Table 1). Obviously, the low 1% threshold includes more small-scale fluctuations in the time-integrated flare area than a threshold of 20%.

3.5. Statistics of Flare Volumes

Thirdly, we histogram the inferred flare volumes V , using the Euclidean definition for a hemisphere with radius L ,

$$V = \frac{2\pi}{3} L^3, \quad (15)$$

which ranges from $V_{min} = 110 \text{ Mm}^3$ to $V_{max} \approx 10^6 \text{ Mm}^3$. The histograms of flare volumes extend over about three orders of magnitude and thus yield a smaller absolute error in the powerlaw slope ($\approx 10\%$) than the distribution of length scales and flare areas. The powerlaw fits are shown separately for each wavelength in Fig. 5c, and the powerlaw slopes are tabulated and averaged in Table 3. The overall average and standard deviation is,

$$\begin{aligned} \alpha_V &= 1.6 \pm 0.2 && \text{Observations} \\ \alpha_V &= 1.67 && \text{Theory (for } d=3) \end{aligned} \quad (16)$$

which also agrees with the predicted value $\alpha_V = 5/3$ for SOC phenomena in 3-D space (Eq. (4); for $d=3$). Also here we find no significant dependence of the powerlaw slope on the wavelength (Fig. 6c, Table 3) or flux threshold (Fig. 7c, Table 3). Thus, the size distribution of volumes does not depend on the flux threshold or observed wavelength.

3.6. Statistics of Flare Durations

For the duration of the 155 analyzed flare events we use the rise time $T = (t_{SXR}^{peak} - t_{SXR}^{start})$ of GOES flares (Fig. 1, top), which reflects the impulsive phase of the flare without the arbitrarily long cooling times in the decay phase of the flare. For the same reason, the duration of energy release cannot easily be determined from EUV data, because the bulk of EUV emission originates late in the postflare phase when the flare plasma cools down to EUV temperatures. The energy release time or impulsive phase of a flare can be best defined by the duration of nonthermal hard X-ray emission $T = (t_{HXR}^{end} - t_{HXR}^{start})$ (Fig. 1, top). Using the Neupert effect, which states that the hard X-rays approximately follow the time derivative of the soft X-rays (as measured by GOES), the peak time t_{peak} of the GOES light curve approximately signals the end of the nonthermal hard X-rays (Fig. 1 top), which justifies that we use the rise time of the soft X-rays as a measure of the energy release time or nonthermal flare duration T . Since the definition of an event duration is most critical for systematic errors and uncertainties of the powerlaw distribution of event durations, we emphasize that the nonthermal flare duration (ignoring the thermal cooling phase) is most consistent with the duration of energy release avalanches in self-organized criticality systems.

The official definition of the flare duration used in the NOAA flare detection algorithm is: The event starts when 4 consecutive 1-minute X-ray values have met all three of the following conditions: (i) All 4 values are above the B1 threshold; (ii) All 4 values are strictly increasing; (iii) The last value is greater than 1.4 times the value that occurred 3 minutes earlier. The peak time is when the flux value reaches

the next local maximum. The event ends when the current flux reading returns to half of the peak value (<http://www.ngdc.noaa.gov/stp/solar/solarflares.html>).

The flare occurrence frequency distribution $N(T)$ of GOES flare durations T is shown in Fig. 5d, which exhibits an approximate powerlaw slope of

$$\begin{aligned} \alpha_T &= 2.1 \pm 0.2 && \text{Observations} \\ \alpha_T &= 2.00 && \text{Theory (for } d = 3) \end{aligned} \quad (17)$$

where we determined a mean and standard deviation from using 10 different trials of histogram binning. This value agrees with the predicted value $\alpha_T = 2$ for SOC phenomena in 3D Euclidean space ($d = 3$) and classical diffusion ($\beta = 1$) according to our FD-SOC model (Eq. 9). While our statistics with a relatively small sample of 155 events is rather humble, larger statistics with over 300,000 GOES flare events has been conducted in Aschwanden and Freeland (2012), where a powerlaw slope of $\alpha_T = 2.02 \pm 0.04$ was found during solar cycle minima, while steeper values are observed during solar cycle maxima, as a consequence of the solar cycle-dependent flare pile-up bias effect.

3.7. Spatio-Temporal Relationships

After we gathered statistics of spatial (L, A, V) and temporal scales T separately, we turn now to spatio-temporal relationships, which we model with a generalized diffusion equation (Eq. 7), specified by a diffusion coefficient κ and a diffusion exponent β . Histograms of the parameters κ and β are shown in Figs. 5f and 7g (for a single threshold of $q_{th} = 0.05$), separately sampled for each of the 7 observed wavelengths λ , and tabulated in Tables 4 and 5.

The diffusion coefficient has a range of values between $\kappa = 4.2$ and $76.7 \text{ Mm s}^{-\beta/2}$, with an overall mean of $\kappa = 29.7 \pm 7.7 \text{ Mm s}^{-\beta/2}$ (Table 4), which shows a slight wavelength dependence within a factor of ≈ 1.5 (Fig. 6f), but no threshold dependence after normalization to a common threshold (Fig. 7f), see Section 3.2.

The diffusion exponent β , for which we expect a value of $\beta = 1$ for classical diffusion, turned out to be sub-diffusive, measured as $\beta = 0.53 \pm 0.27$ for the 335 \AA wavelength in a previous study (Aschwanden 2012b). Here, we confirm the same result of sub-diffusivity, where we find a consistent value of $\beta = 0.50 \pm 0.04$ at the same wavelength of 335 \AA , although we used different flux threshold levels. Averaging over all wavelengths we find also a similar value of $\beta = 0.35 \pm 0.13$ (Table 5). The histograms of the diffusion exponents β show consistent distributions in each of the 7 wavelengths (Fig. 5g), and no particular dependence on the wavelength (Fig. 6g) or flux threshold (Fig. 7g).

In Figure 8 we show scatterplots of those pairs of parameters that have the highest correlation coefficient ($ccc > 0.4$), along with linear regression fits using the *orthogonal reduced major axis* method (Isobe et al. 1990), with the mean and standard deviation of the linear slope indicated. From all possible correlations between the parameters L, T, κ, β , and v_{max} , we find that the highest correlation occurs between the diffusion coefficient κ and the length scale L , with a linear regression fit of

$$\kappa(L) \propto L^{0.94 \pm 0.01}, \quad (18)$$

with a Pearson correlation coefficient of $ccc = 0.96$ (Fig. 8a). This is an unexpected new result, since we assumed an uncorrelated diffusion coefficient κ before. A question of special interest is whether the spatio-temporal data gathered here are consistent with the fractal-diffusive FD-SOC model, which assumes a scaling law of $L \propto T^{\beta/2}$ (Eq. 9). If we investigate a scatterplot, we find indeed a scaling of $L \propto T^{0.46 \pm 0.03}$

(Fig. 8b), which implies, under the assumption of a constant diffusion coefficient κ , a diffusion exponent of $\beta = 0.92 \pm 0.06$, which is consistent with classical diffusion. The correlation between spatial and temporal time scales, however, is weak, with a Pearson correlation coefficient of $ccc = 0.42$ (Fig. 8b).

The best three-parameter correlation actually occurs for the relationship

$$L \propto \kappa T^{0.1} , \quad (19)$$

with a Pearson correlation coefficient of $ccc = 0.97$ (Fig. 9), being valid for all 7 wavelengths (marked with different colors in Fig. 9). Thus, the flare size scale L strongly depends (almost linearly) on the diffusion coefficient κ , but is almost uncorrelated with the time duration T . If we apply the logistic model (Fig. 1 and Eq. 8) instead of the fractal-diffusive model, we indeed expect that the final flare size scale L is proportional to the maximum velocity v_{max} (Eq. 20) and to the diffusion coefficient κ , with no dependence on the duration T in the limit of $T \gg \tau_G$, which is approximately consistent with Eq. (19).

3.8. Statistics of Maximum Velocities

The diffusion equation (Eq. 7) implies a variable expansion speed $v(t)$, but we can define a maximum speed $v_{max} = v(t_1)$ at the transition time t_1 between nonlinear growth and the onset of diffusion (Eq. 8), which is the inflection point of the derivative dr/dt . The maximum velocity v_{max} , occurring at this time t_1 is,

$$v_{max} = \frac{dr}{dt}(t = t_1) = \frac{\kappa\beta}{2}(t_1 - t_k)^{\beta/2-1} = \frac{\beta}{2} \frac{r_1}{(t_1 - t_k)} . \quad (20)$$

Thus, we expect some correlation of the maximum velocity v_{max} with the length scale L and time scale T , by setting $L = r(t = t_1) = r_1$ and $T = (t_1 - t_k)$ in Eq. (20),

$$v_{max} = \frac{\beta}{2} \frac{L}{T} . \quad (21)$$

For the fractal-diffusive model with $L \propto T^{\beta/2}$ this would imply $v_{max} \propto T^{\beta/2-1} \approx T^{-1/2}$ for classical diffusion ($\beta = 1$). However, the scatterplots shown in Fig. 8 exhibit some weak correlations between those parameters, with linear regression fits of $v_{max} \propto T^{-1.1}$ (Pearson correlation coefficient $ccc = 0.43$; Fig. 8c), which is more consistent with the logistic model, where L and T are uncorrelated and $v_{max} \approx T^{-1}$ is expected.

3.9. Fractal Geometry

We explore now the internal geometric structure of solar flares, which we described with a fractal Hausdorff dimension D_d in our FD-SOC model (Eq. 5). We measured the instantaneous flare area $a(t)$ during the flare time interval $[t_{start} < t_i < t_{end}]$ for each of the 155 flares, consisting of typically 100 time frames per flare, by counting the pixels that had a flux in excess of a given flux threshold, for five different thresholds, i.e., $q_{th} = 0.01, 0.02, 0.1, 0.2, 0.5$ of the maximum (preflare background-subtracted) flux during the flare time interval, and for each of the 7 coronal wavelengths. The Euclidean length scale L was determined from the time-integrated flare area $A \propto L^2$ at the end time t_{end} of the flare. The 2-D fractal Hausdorff dimension D_2 was then determined from the relationship $A \propto L^{D_2}$ according to Eq. (5),

$$D_2(t) = \frac{\log A(t)}{\log L} , \quad (22)$$

from which the 3-D fractal dimension $D_3 = (4/3)D_2$ can be inferred. An example of the fractal dimension $D_2(t)$ as a function of time during the flare #28 (the same as shown in Fig. 2) is plotted in Fig. 10. The time-evolution of the fractal dimension $D_2(t)$ can be generally characterized by a rapid initial increase that settles into a constant value after the first impulsive peak of the flare. The example shown in Fig. 10 demonstrates that this behavior is similar at different wavelengths and flux thresholds. The lowest flux thresholds yield at times a slightly higher fractal dimension. We histogram the fractal dimensions for each wavelength in Fig. 5, averaged over all 155 flares and 5 flux thresholds, but separately for each wavelength. Apparently there is no wavelength dependence of the fractal dimension, as the average values show, tabulated in Table 6. Averaging also over all wavelengths, we find a mean value of $D_2 = 1.55 \pm 0.11$ for the 2-D area fractal dimension, and $D_3 = 2.07 \pm 0.26$ for the 3-D volume fractal dimension, which is consistent with the theoretical prediction of the FD-SOC model, with $D_2 = 1.5$ or $D_3 = 2.0$. This is a very useful result that allows us to estimate the emitting flare volume $V = L^{D_3}$ from the flare length scale L , which is relevant for quantifying the observed flux F_λ from the emitting flare volume V .

Note, that the fractal dimension D_3 serves here mostly to estimate the filling factor of the emitting flare plasma. We do not test the self-similarity of the flare geometry at different spatial scales or spatial resolutions for a given flare at a given time here (as measured from a set of 20 large flares in Aschwanden and Aschwanden 2008a,b; or from a cellular automaton avalanche in Aschwanden 2012a), but rather measure the self-similarity as a function of time during a given flare (e.g., Fig. 10), as well as among the entire set of analyzed flares. The so inferred 3-D fractal dimension with a mean and standard deviation of $D_3 = 2.1 \pm 0.3$ is nearly invariant among different flare events, as well as during the main flare time interval (from the peak time t_{peak} to the end time t_{end}).

4. DISCUSSION

4.1. Universal Scaling of Space and Time Parameters

In this Section we discuss observational evidence of our theoretical assumption that the statistical probability distribution functions (PDF) of geometric (or space) and temporal (or time) scales of nonlinear dissipative (avalanche) events in SOC systems are governed by a universal scaling that can be derived from a pure statistical probability argument, regardless of the physical mechanism involved in the generation of a SOC avalanche. This issue is tackled here for the first time with solar data sampled over a broad wavelength and temperature range, and thus over a wide range of physical conditions.

Let us first compare our measurements with previous mostly single-wavelength observations of solar flares. Table 7 offers a compilation of observed size distributions. The most directly measured geometric quantity is the flare area A , while the length $L \propto \sqrt{A}$ (Eq. 11) and volume $V \propto L^3 \propto A^{3/2}$ (Eq. 15) are quantities that are generally derived from the flare area A . For 18 datasets listed in Table 7, frequency distributions for the flare area were measured (Berghmans et al. 1998; Aschwanden et al. 2000; Aschwanden and Parnell 2002; and in this work), with a mean powerlaw slope of $\alpha_A = 2.2 \pm 0.2$, which is consistent with the theoretical prediction $\alpha_A = 2$ (for Euclidean space dimension $d = 3$). Note, that about half of these 18 datasets were measured from nanoflares, while the other half is measured from giant flares (of GOES M- and X-class). So, we find neither a dependence of the flare area distributions $N(A) \propto A^{-\alpha_A}$ on the wavelength λ , nor on the magnitude of the flare, which is also true for the other derived distributions, of length scales $N_L \propto L^{-\alpha_L}$, and volumes $N_V \propto V^{-\alpha_V}$, and thus we can conclude that the size distributions of geometric parameters indeed appear to be universal, at least for the phenomenon of solar flares, as the compilation

with a number of different instruments and wavelength ranges demonstrates in Table 7. Additional support for the universality of the powerlaw slope of $\alpha_L \approx 3$ is also given by the size distributions of lunar craters, asteroids, and Saturn ring particles, which have been associated with SOC mechanisms (Aschwanden 2013).

Size distributions of time scales T were measured for a larger number of datasets (Crosby et al. 1993, 1998; Lu et al. 1993; Lee et al. 1993; Bromund et al. 1995; Berghmans et al. 1998; Aschwanden et al. 2000; Veronig et al. 2002; McIntosh and Gurman 2005; Su et al. 2006; Yashiro et al. 2006; Christe et al. 2008; Nishizuka et al. 2009; Aschwanden 2011, 2012b; Aschwanden and Freeland 2012; and in this work), as listed in Table 7. If we exclude those measurements that fitted a broken powerlaw (Crosby et al. 1998; Georgoulis et al. 2001; Su et al. 2006), a powerlaw with an exponential fall-off (McIntosh and Gurman 2005), or those without preflare background subtraction (Veronig et al. 2002; Yashiro et al. 2006), we have 20 independently measured datasets with a mean powerlaw slope of $\alpha_T = 2.3 \pm 0.4$, which is consistent with the theoretical prediction $\alpha_T = 2$. These time scale distributions $N(T) \propto T^{-\alpha_T}$ have been measured from photons with different emission mechanisms, such as nonthermal bremsstrahlung at hard X-ray energies of > 25 keV, or thermal line emission in soft X-rays ($1 - 8$ Å) and EUV wavelengths ($94 - 335$ Å). The fact that we measure the same powerlaw slope for different physical emission mechanisms, which is moreover consistent with the probability distribution $N(T) \propto T^{-2}$ predicted by the FD-SOC model, strongly supports the interpretation that the time scale distribution has universal validity also, depending only on the Euclidean dimension ($d = 3$) of the length scale distribution $N(L) \propto L^{-d}$ and on the random walk statistics $L \propto T^{1/2}$ that defines the spatio-temporal transport process.

4.2. Finite-Size Effects of Active Regions

Solar flares do not occur uniformly distributed over the entire solar surface, but are generated in active regions only, where strong magnetic fields emerge, generated by the internal solar dynamo. Every active region thus represents a finite-size SOC system, limiting also the maximum size of solar flares. In our measured distribution of flare length scales L , defined from the radius of a circular area that is equivalent to the observed flare area $A = \pi L^2$, we find a range of approximately $L \approx 5 - 100$ Mm (Figs. 5a and 9), which corresponds to diameters in the range of $2L = 10 - 200$ Mm for circular flare areas. If the flare area is highly elongated, the major axis can be factor of $\lesssim 5$ longer than the minor axis. One of the largest observed flares is the Bastille-Day flare, which has an arcade length of $l \approx 180$ Mm and a width of $w \approx 35$ Mm (Aschwanden and Alexander 2001), which indeed has an elongation factor of $l/w \approx 5$. The largest flare we observed in our selection has a diameter of $2L \lesssim 200$ Mm, which amounts to about a quarter of the solar radius, corresponding to the largest active regions seen on the Sun (e.g., Tang et al. 1984). Thus, the size of flares can occupy almost entire active regions, and consequently we would expect finite-size effects that limit the upper boundary of the size distribution, and potentially could produce a bump at the upper cutoff of the size distribution (e.g., as it happens for auroral blobs; Lui et al. 2000). Such an effect is not evident in our data (Fig. 5a) and has not been reported somewhere else, which suggests that there is no significant number of giant flares that reach the full size of active regions. Moreover, the largest flares occur in active regions of different sizes, which smears out the upper cutoffs in the combined size distributions of flares. This is an important detail that effects the forecasting of the most extreme (space weather) events.

4.3. Solar Cycle Effects

Although the size distribution of flare durations can be considered as universal, there is a non-universal effect that is caused by the solar cycle, which controls the variation of the flare rate over several orders of magnitude, from the minimum to the maximum of the solar magnetic 11-year cycle. This effect was most clearly measured in a large sample of over 300,000 solar flares detected with GOES during the last 37 years (Aschwanden and Freeland 2012). The flare rate during the solar maximum increases to a level that does not warrant the separation of time scales anymore, i.e., the waiting times (i.e., the time intervals between subsequent flares) are not any longer much larger than the flare durations, and thus subsequent flare events start to pile-up, which leads to an under-estimate of the true duration of large flares (since the previous flare has to end before the next flare starts in most automated flare detection algorithms). A consequence of such a fast-driven system is a steepening of the size distribution of flare durations during times of high flare rates. The study of Aschwanden and Freeland (2012) has demonstrated that the powerlaw slope of flare durations amounts to a lowest value of $\alpha_T = 2.02 \pm 0.04$ in years the near solar minimum, close to the theoretical expectation of $\alpha_T = 2$, but to a much steeper value during solar maxima, approaching values as high as $\alpha_T \lesssim 5$ during the most flare-active years. Nevertheless, this is mostly a technical detection problem and could in principle be eliminated if the true flare duration would be measured during times of high flare rates by modeling the time profiles in the decay phase beyond the overlap with the next flare. So, it is a measurement problem only, rather than a non-universal property of the size distribution of event durations in solar flares.

4.4. Effects of CMEs and EUV Dimming

Investigating the measured flare area size distributions $N(A)$ in 7 different wavelengths and in 5 different flux thresholds (Figs. 4, 6b, 7b), as well as the powerlaw slopes listed in Tables 1, 2, and 3 for lengths L , areas A , and volumes V , it becomes apparent that the largest deviations from the averages occur in the wavelengths of 171 and 193 Å, especially at the lowest flux thresholds of $q_{th} = 0.01$ and 0.02. Inspecting the flare movies in those wavelengths it becomes clear that these wavelengths show most prominently the EUV dimming that is caused after the “evacuation” of a coronal mass ejection (CME), leading to an underestimate of the flare-related EUV emission. Since up to 84% of CMEs exhibit EUV dimming (Bewsher et al. 2008), this is quite common, and shows up as a double-peaked size distribution of flare areas in the wavelengths of 171 and 193 Å (Fig. 4). This is an additional non-universal effect that is idiosyncratic to solar flares associated with CMEs. An analogy to Bak’s sandpile paradigm of SOC systems would be huge sand avalanches that cause an additional dust storm which occults part of the avalanche, and thus would affect the accuracy in the measurement of sand avalanche sizes. In order to obtain accurate size distributions of solar flares, we thus recommend to avoid the 171 and 193 Å wavelengths, at least not for large eruptive flares, where the percentage of CMEs and EUV dimming is highest (Andrews 2003; Yashiro et al. 2005; Wang and Zhang 2007; Cheng et al. 2010).

4.5. Eruptive Versus Confined Flares

The spatio-temporal relationship $L(T) = \kappa T^{\beta/2}$ (Eq. 7) is quantified by a generalized diffusion process in our FD-SOC framework. Interestingly, the diffusion coefficients κ and diffusion (or spreading) exponents β appear not to be constant for the analyzed sample of large flares, but show a rather large variation from

sub-diffusion to classical diffusion (statistical random walk), while a few events are even in the hyper-diffusive regime. In order to gain more physical insight into this behavior, we consulted a flare classification catalog of the same 155 analyzed events that was established by Zhang and Liu (2012). In this catalog, GOES M- and X-class flares, analyzed from SDO, SOHO, and STEREO data, were classified based on their association with CMEs, or lack of CMEs, into eruptive versus confined flares. An eruptive flare is defined strictly as a flare associated with a coronal mass ejection (CME) seen in coronagraph images, while a confined flare exhibits no noticeable CME. The verification of the flare type is carried out straightforwardly through direct comparison with concurrent coronagraph images, and coronal EUV images as well. For each of the major SDO flares, the SOHO/LASCO images were carefully checked for a possible association with a CME, and potential disk signatures were also checked in AIA/SDO images, including flare brightenings, EUV dimming, and post-eruption arcades. In some cases, when necessary, STEREO/COR2 coronagraph images and EUVI coronal images were checked in addition for further verification. Therefore, the classification of flares into eruptive and confined types is believed to be unambiguous. Previous studies have shown that about 90% of X-class flares and about 50% of M-class flares are associated with CMEs; in other words, 10% of X-class flares and 50% of M-class flares are confined (Andrews 2003; Yashiro et al. 2005; Wang and Zhang 2007; Cheng et al. 2010). From the 155 events analyzed in this study, we have an overlap of 125 events with the catalog of Zhang and Liu (2012), for which we find 59 eruptive (47%) and 66 confined (53%) flare events.

In Fig. 11 we show histograms of the various measured parameters ($L, V, T_{AIA}, F_{GOES}, T_{GOES}, v_{max}, F_{AIA}, \kappa, \beta$) at a wavelength of 335 Å, separated into the two groups of eruptive flares (Fig. 11, white histograms) and confined flares (Fig. 11, grey histograms). Interestingly, we find significant differences in the parameter distributions for flare volumes V , GOES durations T_{GOES} , EUV fluxes F_{AIA} , and in the diffusion coefficient κ . Eruptive flares have larger volumes V , longer soft X-ray durations T_{GOES} , larger EUV fluxes F_{AIA} , and somewhat larger diffusion coefficients κ . The differences between eruptive and confined flares are very similar in all 7 analyzed wavelengths (Fig. 11 shows only one of them, i.e., 335 Å). Some of these differences are expected according to some theoretical CME models. For instance, eruptive events are expected to have a more expansive dynamics, and thus a larger diffusion coefficient than the confined ones, which are more stationary flare events, occurring within a closed-field magnetic configuration. Eruptive events seem also to release more magnetic energy than confined flares, leading to statistically larger volumes V and fluxes (F_{SXR}, F_{AIA}).

4.6. Diffusion Spreading Coefficient and Long-Range Correlations

We described the results of the spatio-temporal relationships in Section 3.7 and showed the correlations among different parameters in Fig. 8. The most remarkable correlation, which gives us the best hint of a hidden scaling law is the almost linear relationship $\kappa \propto L^{0.94 \pm 0.01}$ (Eq. 18) between length scales L and diffusion coefficients κ (Fig. 8, panel a). The uncertainty in the linear regression coefficient amounts to only $\approx 1\%$. Including also a possible dependence on the time duration T , which is expected from random-walk transport processes, we find an equally tight three-parameter correlation $L \propto \kappa T^{0.1}$ (Fig. 9). Since the spatio-temporal evolution fits $L(t) = \kappa T^{\beta/2}$ (e.g., Fig. 2, middle panel) are most consistent with a constant diffusion coefficient per flare event and subdiffusive spreading exponents of $\beta = 0.35 \pm 0.13$ (Table 5), the statistical correlation among many flare events is dominated by the diffusion coefficient κ rather than by the spreading exponent β . Therefore, flare events that have a small diffusion coefficient κ expand to relatively small spatial scales L , while other events with large local diffusion coefficients κ produce the largest flare sizes. The diffusion coefficient κ is therefore the most critical and most controlling parameter of the flare

size L .

In SOC systems, a critical threshold determines whether a nonlinear dissipation event starts or not, while the size of a SOC avalanche is mostly controlled by the spatio-temporal correlation characteristics (Eq. 1) of the SOC system. Locations with long-range correlation lengths produce predictably larger SOC avalanches. Long-range correlations become important when significant deviations from the critical threshold extend over a larger spatial area or volume. This is another way of saying that a SOC system self-organizes to the *vicinity of a critical state*, rather than being exactly at the critical threshold. We illustrate this behavior with the sandpile analogy in Fig. 12 (left). The slope of a critical sandpile shows coarse-graininess and significant deviations from the critical slope, especially in places that have been eroded from previous large avalanches, which can be quantified by a cross-correlation function $C(x, t)$ that exhibits significant long-range correlation lengths in extended deviant locations (Fig. 12, left). Subsequent avalanches triggered in those deviant sub-critical locations may evolve predictably into relatively large SOC avalanches. In the situation of solar flares, the non-potential magnetic field component B_{NP} plays the same critical role as the repose angle or slope of the sandpile. Extended locations with coherent non-potential fields (Fig. 12, right) exhibit long-range correlation lengths and are more likely to product larger avalanches subsequently. Observations have shown that the length of the neutral line segment with highly sheared and stressed magnetic fields is a good predictor of flares (e.g., Schrijver 2007, Falconer et al. 2011, 2012). The curl of the non-potential field corresponds to the electric current density $\mathbf{j}/4\pi = \nabla \times \mathbf{B}_{NP}$ that drives the dissipation of magnetic energy during flares, once it exceeds a critical threshold $|\mathbf{j}| \geq j_{\text{crit}}$ (e.g., Vassiliadis et al. 1998; Isliker et al. 1998a, 2000, 2001; Galsgaard 1996; Morales and Charbonneau 2008a, b, 2009). It is therefore important to develop reliable *nonlinear force-free magnetic field (NLFFF)* models that measure the spatial and temporal distribution of the current density $\mathbf{j}(\mathbf{x}, t)$ in active regions, which map out long-range correlation lengths that are susceptible to areas where large flares are most likely to occur, a task that is at the heart of forecasting centers that aim to predict large and extreme (space weather) events. SOC systems may provide in this way not only statistical overall probabilities of events, but also probabilities for sizes and start times of individual single events. In order to achieve this, future studies should focus on characterizing relationships between current distributions $\mathbf{j}(\mathbf{x}, t)$ derived from NLFFF models and the diffusion (or spreading) exponent κ that can be measured by fitting the generalized diffusion equation $r(t) = \kappa(t - t_k)^{\beta/2}$ (Eq. 7) as performed in this study.

5. CONCLUSIONS

In this study we analyzed the spatio-temporal evolution of a statistically complete data set (of GOES M- and X-class flares observed with AIA/SDO during the first two years of the mission), from which we measure geometric parameters (lengths, areas, volumes, fractal area dimensions), temporal parameters (flare durations), and spatio-temporal parameters (diffusion coefficient, diffusion or spreading powerlaw exponent, maximum diffusion velocity). In this study we expanded a previous single-wavelength (335 Å) study (Aschwanden 2012b) to the entire range of 7 coronal wavelengths of AIA (94, 131, 171, 193, 211, 304, 335 Å), and generalize the flare area definition by including 5 different flux threshold levels. In addition we make use of a flare catalog that provides a classification into eruptive and confined flares (Zhang and Liu 2012). The statistical distributions obtained in this study are compared with the predictions from the theory of the fractal-diffusive avalanche model of a slowly-driven self-organized criticality system (Aschwanden 2012a). The major conclusions of this statistical study are:

1. The spatio-temporal evolution of flares can be satisfactorily fitted in all events and in all coronal wavelengths with the generalized diffusion model, which includes an initial acceleration phase with exponential growth, followed by a deceleration phase with diffusive random-walk characteristics $r(t) = \kappa(t - t_k)^{\beta/2}$. We find a mean diffusion coefficient of $\kappa = 30 \pm 8$ Mm $s^{\beta/2}$ and a mean diffusion (or spreading) exponent of $\beta = 0.35 \pm 0.13$, which is in the sub-diffusive regime (likely to be caused by the anisotropy of the magnetic field in the flare regions).
2. The strongest correlation among spatio-temporal parameters is found between the flare length scale L and the diffusion coefficient κ , i.e., $\kappa \propto L^{0.94 \pm 0.01}$, which combined with the weaker correlation with time scales T , i.e., $L \propto T^{0.46 \pm 0.03}$, being consistent with classical random walk diffusion, leads to the 3-parameter scaling law $L \approx \kappa T^{0.1}$. We interpret the strong correlation between flare size L and the diffusion coefficient κ in terms of long-range correlation lengths in the vicinity of a self-organized criticality state, predicting a physical relationship between the local diffusion coefficient κ and the non-potential magnetic field component B_{NP} , which can be used for forecasting of flare sizes L by analyzing the pre-flare non-potential magnetic field.
3. The observed size distributions of geometric (L, A, V, D_d) and temporal parameters (T) are consistent with the theoretical predictions of the FD-SOC model, i.e., $N(L) \propto L^{-3}$, $N(A) \propto A^{-2}$, $N(V) \propto V^{-5/3}$, $N(T) \propto T^{-2}$, $D_2 = 3/2$, and $D_3 = 2$ for a Euclidean dimension of $d = 3$, and thus confirm the scale-free probability conjecture and the fractal random walk diffusivity assumption of the FD-SOC model. While this agreement of the powerlaw slopes between observations and theoretical predictions has been shown in one single wavelength earlier (Aschwanden 2012b), we demonstrate the same agreement here for all coronal wavelengths observed with AIA and thus conclude that the powerlaw slopes of the geometric and spatial size distributions predicted by the FD-SOC model have universal validity, independent of other physical parameters such as electron densities, electron temperatures, or wavelengths.
4. The size range of the analyzed flares, which represent the largest events (GOES M- and X-class) occurring on the Sun, are found to cover a (diameter) range of $2L \approx 10 - 200$ Mm, which is close to the size of the largest active regions on the Sun. However, we do not find any evidence for finite-size effects of SOC systems that would modify the upper cutoff of the powerlaw-like size distributions.
5. Non-universal effects that affect the size distribution of solar flares are found to result from CMEs and the associated EUV dimming, which leads to underestimates of the EUV flux in wavelengths of 171 and 193 Å, producing a double-peaked size distribution. Also the solar cycle can affect the powerlaw slope of measured size distributions of flare durations T , which are systematically underestimated due to flare pile-up during episodes of high flaring rates, as they occur during the solar maximum (Aschwanden and Freeland 2012).
6. Eruptive flares (associated with a CME) have larger volumes V , longer soft X-ray durations T_{GOES} , larger EUV fluxes F_{AIA} , and somewhat larger diffusion coefficients κ than confined flares (without accompanying CME). Eruptive events seem to release more magnetic energy than confined flares, leading to statistically larger volumes V and fluxes (F_{SXR}, F_{AIA}).

The major satisfaction of these results is our increasing understanding of the universality of self-organized criticality systems. We understand now the perplexing question why we observe powerlaw distributions in nature in the first place, in contrast to Gaussian distributions. Gaussian or exponential distributions indicate incoherent processes that cannot explain extreme (“king-dragon” or “black-swan”) events in the “fat tail”

of probability distribution functions, while powerlaw distributions are naturally obtained from the scale-free probability conjecture (Eq. 2), which occur due to the coherent nature of multiplicative chain reactions, requiring long-range correlation lengths (Eq. 1) in the vicinity of a self-critical state. A logical next step is the study of relationships between long-range correlation of SOC-critical parameters, such as the nonpotential magnetic field $\mathbf{B}_{NP}(\mathbf{x}, t)$ in solar flaring regions, and the magnitude or size L of occurring solar flares, which is found to be directly proportional to the diffusion spreading exponent κ . Besides the universality of scaling laws for space and time parameters in SOC systems, there are also non-universal scaling laws that depend directly on the relationship between observables (such as fluxes in different wavelengths) and the geometric avalanche (or flare) volume, which will be pursued in Paper II. In future studies, the statistics of flare events should be extended from the giant flares analyzed here, to the smaller microflares and nanoflares, in order to improve the accuracy of the measured powerlaw slopes (over several decades) and to test over what maximum range of parameter space the same physical scaling laws are valid.

The author acknowledges helpful discussions and software support of the AIA/SDO team, as well as constructive comments by anonymous referees. This work has benefitted from fruitful discussions with Henrik Jensen, Nicholas Watkins, Jürgen Kurths, and by the *International Space Science Institute (ISSI)* at Bern Switzerland, which hosted and supported a workshop on *Self-Organized Criticality and Turbulence* during October 15-19, 2012. This work was partially supported by NASA contract NNX11A099G “Self-organized criticality in solar physics” and NASA contract NNG04EA00C of the SDO/AIA instrument to LMSAL.

REFERENCES

- Andrews, M.D. 2003, Sol. Phys.218, 261.
- Aschwanden, M.J., Tarbell, T., Nightingale, R., Schrijver, C.J., Title, A., Kankelborg, C.C., Martens, P.C.H., and Warren,H.P., 2000, ApJ 535, 1047.
- Aschwanden, M.J. and Alexander, D. 2001, Sol. Phys.204, 91.
- Aschwanden, M.J., Parnell, C.E. 2002, ApJ 572, 1048.
- Aschwanden, M.J. and Aschwanden, P.D. 2008a, ApJ674, 530.
- Aschwanden, M.J. and Aschwanden, P.D. 2008b, ApJ674, 544.
- Aschwanden, M.J. 2011, *Self-Organized Criticality in Astrophysics. The Statistics of Nonlinear Processes in the Universe*, ISBN 978-3-642-15000-5, Springer-Praxis: New York, 416p.
- Aschwanden, M.J. 2012a, A&A, 539, A2.
- Aschwanden, M.J. 2012b, ApJ, 757, 94.
- Aschwanden, M.J. and Freeland, S.L. 2012, ApJ, 754, 112.
- Aschwanden, M.J. (Ed.) 2013, “*Self-Organized Criticality Systems*”, Open Academic Press, Warsaw, Berlin; <http://www.openacademicpress.de/>, 483pp.
- Bak, P., Tang, C., and Wiesenfeld, K. 1987, Physical Review Lett. 59/27, 381.
- Bak, P., Tang, C., and Wiesenfeld, K. 1988, Physical Review A 38/1, 364.
- Bak, P., and Chen, K. 1989, J. Phys. D., 38, 5.
- Berghmans, D., Clette, F., and Moses, D. 1998, A&A, 336, 1039.

- Bewsher, D., Harrison, R.A., Brown, D.S. 2008, A&A478, 897.
- Boerner, P., Edwards, C., Lemen, J., Rausch, A., Schrijver, C., Shine, R., Shing, L., Stern, R., Tarbell, T., Title, A., Wolfson, C. J., Soufli, R., Spiller, E., Gullikson, E., McKenzie, D., Windt, D., Golub, L., Podgorski, W., Testa, P., and Weber, M. 2012, Sol. Phys.275, 41.
- Bromund, K.R., McTiernan, J.M., and Kane, S.R. 1995, ApJ 455, 733.
- Cheng, X., Zhang, J., Ding, M.D., Poomvises, 2010, ApJ712, 752.
- Christe, S., Hannah, I.G., Krucker, S., McTiernan, J., and Lin, R.P. 2008, ApJ 677, 1385.
- Crosby, N.B., Aschwanden, M.J., and Dennis, B.R., 1993, Sol. Phys.143, 275.
- Crosby, N.B., Vilmer, N., Lund, N., and Sunyaev, R. 1998, A&A334, 299.
- Dennis, B.R. 1985, Sol. Phys.100, 465.
- Falconer, D.A., Barghouty, A.F., Khazanov, I., and Moore, R. 2011, Space Weather Journal, 9/4, CiteID S04003.
- Falconer, D.A., Moore, R.L., Barghouty, A.F., and Khazanov, I. 2012, ApJ 757, 32.
- Galsgaard, K. 1996, A&A315, 312.
- Georgoulis, M.K., Vilmer, N., Crosby, N.B. 2001, AA 367, 326.
- Isliker, H., Anastasiadis, A., Vassiliadis, D., and Vlahos, L. 1998, A&A335, 1085.
- Isliker, H., Anastasiadis, A., and Vlahos, L. 2000, A&A363, 1134.
- Isliker, H., Anastasiadis, A., and Vlahos, L. 2001, A&A377, 1068.
- Isobe, T., Feigelson, E.D., Akritas, M., and Babu, G.J. 1990, ApJ364, 104.
- Jensen, H. 1998, *Self-Organized Criticality: Emergent complex behaviour in physical and biological systems*, Cambridge University Press.
- Lee, T.T., Petrosian, V., and McTiernan, J.M. 1993, ApJ 412, 401.
- Lemen, J.R. et al. 2012, Sol. Phys., 275, 17.
- Lu, E.T. and Hamilton, R.J. 1991, ApJ 380, L89.
- Lu, E.T., Hamilton, R.J., McTiernan, J.M. and Bromund, K.R. 1993, ApJ 412, 841.
- Lui, A.T.Y., Chapman, S.C., Liou, K., Newell, P.T., Meng, C.I., Brittnacher, M., and Parks, G.K. 2000, GRL 27/7, 911.
- McIntosh, S.W., and Gurman, J.B. 2005, Sol. Phys.228, 285.
- Mandelbrot, B.B. 1982, *The Fractal Geometry of Nature*, ISBN 0-7167-186-9, W.H. Freeman.
- Morales, L. and Charbonneau, P. 2008a, ApJ682, 654.
- Morales, L. and Charbonneau, P. 2008b, Geophys. Res. Lett.35, 4108.
- Morales, L. and Charbonneau, P. 2009, ApJ698, 1893.
- Nishizuka, N., Asai, A., Takasaki, H., Kurokawa, H., and Shibata, K. 2009, ApJ 694, L74.
- Pruessner, G. 2012, *Self-Organised Criticality. Theory, Models and Characterisation*, Cambridge University Press, Cambridge.
- Schrijver, C.J. 2007, ApJ655, L117.
- Su, Y.N., Gan, W.Q., and Li, Y.P. 2006, Sol. Phys.238, 61.

- Tang, F., Howard, R., and Adkins, J.M. 1984, Sol. Phys.91, 75.
- Vassiliadis, D., Anastasiadis, A., Georgoulis, M., and Vlahos L. 1998, ApJ509, L53.
- Veronig, A.M., Temmer, M., Hanslmeier, A., Otruba, W., and Messerotti, M. 2002, A&A382, 1070.
- Wang, Y., Zhang, J. 2007, ApJ665, 1428.
- Yashiro, S., Gopalswamy, N., Akiyama, N., Michalek, S., and Howard, R. A. 2005, JGR 110, A12S05.
- Yashiro, S., Akiyama, S., Gopalswamy, N., and Howard, R. A. 2006, ApJ 650, L143.
- Zhang, Jie and Liu, K. 2012, “Zoology of Solar Eruptions”, AAS Meeting 2012, Abstract #220, #204.45.

Table 1. Statistics of powerlaw slopes α_L of length scales L[Mm] of 155 solar flares, tabulated in 7 AIA wavelengths and for 5 different flux thresholds. The theoretical prediction of the FD-SOC model is $\alpha_L = 3$.

Wavelength [Å]	Threshold 1%	Threshold 2%	Threshold 5%	Threshold 10%	Threshold 20%	All
94	3.4	3.6	2.2	3.2	2.9	3.1± 0.6
131	3.7	4.2	3.6	3.3	2.8	3.5± 0.5
171	5.2	4.2	3.0	2.4	2.8	3.5± 1.2
193	4.9	3.8	2.9	2.9	3.0	3.5± 0.9
211	3.7	2.6	2.3	2.2	2.5	2.7± 0.6
304	3.9	3.1	2.9	2.6	2.3	2.9± 0.6
335	3.4	3.3	3.2	2.4	3.2	3.1± 0.4
All	4.0± 0.7	3.6± 0.6	2.9± 0.5	2.7± 0.4	2.8± 0.3	3.2± 0.7

Table 2. Statistics of powerlaw slopes α_A of flare areas A[Mm²] of solar flares, tabulated for 7 different AIA wavelengths and 5 different flux thresholds. The theoretical prediction of the FD-SOC model is $\alpha_A = 2$.

Wavelength [Å]	Threshold 1%	Threshold 2%	Threshold 5%	Threshold 10%	Threshold 20%	All
94	2.0	2.2	1.8	2.0	2.1	2.0± 0.1
131	2.4	2.2	2.2	2.2	1.9	2.2± 0.2
171	2.8	2.6	1.9	1.6	1.7	2.1± 0.5
193	2.6	2.1	1.8	1.8	1.7	2.0± 0.3
211	2.4	2.2	1.8	1.9	1.6	2.0± 0.4
304	2.2	2.3	2.1	2.1	1.9	2.1± 0.2
335	2.1	2.2	1.8	2.0	1.7	1.9± 0.2
All	2.4± 0.3	2.2± 0.2	1.9± 0.2	2.0± 0.2	1.8± 0.2	2.1± 0.3

Table 3. Statistics of powerlaw slopes α_V of flare volumes V[Mm³] of solar flares, tabulated for 7 different AIA wavelengths and 5 different flux thresholds. The theoretical prediction of the FD-SOC model is $\alpha_V = 5/3 \approx 1.67$.

Wavelength [Å]	Threshold 1%	Threshold 2%	Threshold 5%	Threshold 10%	Threshold 20%	All
94	1.6	1.4	1.5	1.6	1.6	1.5± 0.1
131	1.9	1.9	1.7	1.7	1.4	1.7± 0.2
171	2.0	1.8	1.5	1.4	1.5	1.7± 0.2
193	2.0	1.9	1.5	1.5	1.6	1.7± 0.2
211	1.8	1.7	1.6	1.6	1.4	1.6± 0.2
304	1.8	1.8	1.7	1.8	1.4	1.7± 0.1
335	1.6	1.6	1.6	1.5	1.7	1.6± 0.1
All	1.8± 0.2	1.7± 0.2	1.6± 0.1	1.6± 0.1	1.5± 0.1	1.6± 0.2

Table 4. The diffusion coefficient κ [$\text{Mm s}^{-\beta/2}$] of 155 solar flares is tabulated for 7 different AIA wavelengths and 5 different flux thresholds.

Wavelength [\AA]	Threshold 1%	Threshold 2%	Threshold 5%	Threshold 10%	Threshold 20%	All
94	19	21	22	23	23	21 ± 2
131	23	25	28	30	31	27 ± 3
171	46	41	36	35	35	39 ± 5
193	43	40	39	39	41	40 ± 2
211	33	30	30	31	32	31 ± 1
304	29	27	28	28	28	28 ± 1
335	19	19	20	21	20	20 ± 1
All	30 ± 11	29 ± 9	29 ± 7	30 ± 6	30 ± 7	30 ± 8

Table 5. The diffusion exponent β of 155 solar flares is tabulated for 7 different AIA wavelengths and 5 different flux thresholds. The theoretical prediction of the FD-SOC model is $\beta = 1$ for classical diffusion.

Wavelength [\AA]	Threshold 1%	Threshold 2%	Threshold 5%	Threshold 10%	Threshold 20%	All
94	0.44	0.45	0.45	0.42	0.39	0.43 ± 0.03
131	0.26	0.27	0.28	0.26	0.16	0.25 ± 0.05
171	0.48	0.47	0.43	0.39	0.37	0.43 ± 0.05
193	0.36	0.24	0.18	0.16	0.19	0.23 ± 0.08
211	0.47	0.06	0.42	0.43	0.28	0.33 ± 0.17
304	0.36	0.34	0.32	0.30	0.03	0.27 ± 0.14
335	0.56	0.50	0.49	0.52	0.44	0.50 ± 0.04
All	0.42 ± 0.10	0.33 ± 0.16	0.37 ± 0.11	0.35 ± 0.12	0.27 ± 0.15	0.35 ± 0.13

Table 6. Statistics of fractal dimensions D_2 of solar flare areas tabulated for 7 different AIA wavelengths and 5 different flux thresholds. The theoretical prediction of the FD-SOC model is $D_2 = 3/2$.

Wavelength [\AA]	Threshold 1%	Threshold 2%	Threshold 5%	Threshold 10%	Threshold 20%	All
94	1.7	1.7	1.6	1.6	1.5	1.6 ± 0.1
131	1.7	1.7	1.6	1.6	1.5	1.6 ± 0.1
171	1.7	1.6	1.5	1.4	1.3	1.5 ± 0.1
193	1.7	1.7	1.6	1.6	1.5	1.6 ± 0.1
211	1.7	1.6	1.6	1.5	1.4	1.6 ± 0.1
304	1.6	1.6	1.5	1.4	1.2	1.5 ± 0.2
335	1.6	1.6	1.5	1.4	1.3	1.5 ± 0.1
All	1.7 ± 0.1	1.6 ± 0.1	1.6 ± 0.1	1.5 ± 0.1	1.4 ± 0.1	1.6 ± 0.1

Table 7. Size distributions of geometric and temporal parameters in solar flares.

Instrument	Wavelength or energy λ, ϵ	Number of events N	Length exponent α_L	Area exponent α_A	Volume exponent α_V	Duration exponent α_T	Reference
SMM/HXRBS	>25 keV	7045				2.17±0.05	Crosby et al. (1993)
SMM/HXRBS	>25 keV	1008				1.95±0.09	Crosby et al. (1993)
SMM/HXRBS	>25 keV	545				2.22±0.13	Crosby et al. (1993)
SMM/HXRBS	>25 keV	3874				1.99±0.06	Crosby et al. (1993)
ISEE-3	>25 keV	4356				1.88	Lu et al. (1993)
ISEE-3	>25 keV	4356				2.73	Lee et al. (1993)
ISEE-3	>25 keV	4356				2.40±0.04	Bromund et al. (1995)
GRANAT/WATCH	>10 keV	1551				1.09-2.28 ^a	Crosby et al. (1998)
SOHO/EIT	304 Å	13,067		2.7		3.1	Berghmans et al. (1998)
SOHO/EIT	195 Å	13,607		2.0		2.1	Berghmans et al. (1998)
TRACE	171-195 Å	281	2.10±0.11	2.56±0.23	1.94±0.09		Aschwanden et al. (2000)
GRANAT/WATCH	>10 keV	1518 Å				1.15-2.25 ^a	Georgoulis et al. (2001)
TRACE/C	171-195 Å		3.24±0.16	2.43±0.10	2.08±0.07		Aschwanden and Parnell (2002)
TRACE/A	171 Å	436	2.87±0.24	2.45±0.09	1.65±0.09		Aschwanden and Parnell (2002)
TRACE/B	171 Å	436	2.77±0.17	2.34±0.10	1.75±0.13		Aschwanden and Parnell (2002)
TRACE/A	195 Å	380	2.59±0.19	2.16±0.18	1.69±0.05		Aschwanden and Parnell (2002)
TRACE/B	195 Å	380	2.56±0.17	2.24±0.04	1.63±0.04		Aschwanden and Parnell (2002)
Yohkoh/SXT	AlMg	103	2.34±0.27	1.86±0.13	1.44±0.07		Aschwanden and Parnell (2002)
TRACE+SXT	171,195,AlMg	919	2.41±0.09	1.94±0.03	1.55±0.03		Aschwanden and Parnell (2002)
GOES	1-8 Å	49,409				2.93±0.12 ^c	Veronig et al. (2002)
SONO/EIT	195 Å	200,000				1.4-2.0 ^b	McIntosh and Gurman (2005)
RHESSI	12 – 25keV	2649				0.9-3.56 ^c	Su et al. (2006)
GOES	1-8 Å	1365				2.87±0.09 ^c	Yashiro et al. (2006)
GOES	1-8 Å					2.49±0.11 ^c	Yashiro et al. (2006)
GOES	1-8 Å					3.22±0.15 ^c	Yashiro et al. (2006)
RHESSI	6-12 keV	25705				2.2±0.18	Christe et al. (2008)
TRACE	1550 Å					2.3	Nishizuka et al. (2009)
SMM/HXRBS	>25 keV	11,549				2.05	Aschwanden (2011)
CGRO/BATSE	>25 keV	4109				2.20	Aschwanden (2011)
RHESSI	>25 keV	11,595				2.00	Aschwanden (2011)
GOES	1-8 Å	255,474				3.20±0.04 ^d	Aschwanden and Freeland (2012)
GOES	1-8 Å	67,296				2.75±0.02 ^e	Aschwanden and Freeland (2012)
GOES	1-8 Å	18,676				2.26±0.01 ^f	Aschwanden and Freeland (2012)
GOES	1-8 Å	155				1.92	Aschwanden (2012b)
AIA/SDO	335 Å	155	1.96			2.17	Aschwanden (2012b)
GOES	1-8 Å	155				2.10±0.18	This work
AIA/SDO	94 Å	155	3.1±0.6	2.0±0.1	1.5±0.1		This work
AIA/SDO	131 Å	155	3.5±0.5	2.2±0.2	1.7±0.2		This work
AIA/SDO	171 Å	155	3.5±1.2	2.1±0.5	1.7±0.2		This work
AIA/SDO	193 Å	155	3.5±0.9	2.0±0.3	1.7±0.2		This work
AIA/SDO	211 Å	155	2.7±0.6	2.1±0.3	1.6±0.2		This work
AIA/SDO	304 Å	155	2.9±0.6	2.1±0.2	1.7±0.1		This work
AIA/SDO	335 Å	155	3.1±0.4	1.9±0.2	1.6±0.1		This work
AIA/SDO	94-335 Å	155	3.2±0.7	2.1±0.3	1.6±0.2		This work
Theory			3.00	2.00	1.67	2.00	

^aDouble-powerlaw fit.

^bPowerlaw fit with exponential fall-off.

^cNo preflare background flux subtraction.

^dDuring solar cycle minima years.

^eDuring intermediate solar cycle years.

^fDuring solar cycle maxima years.

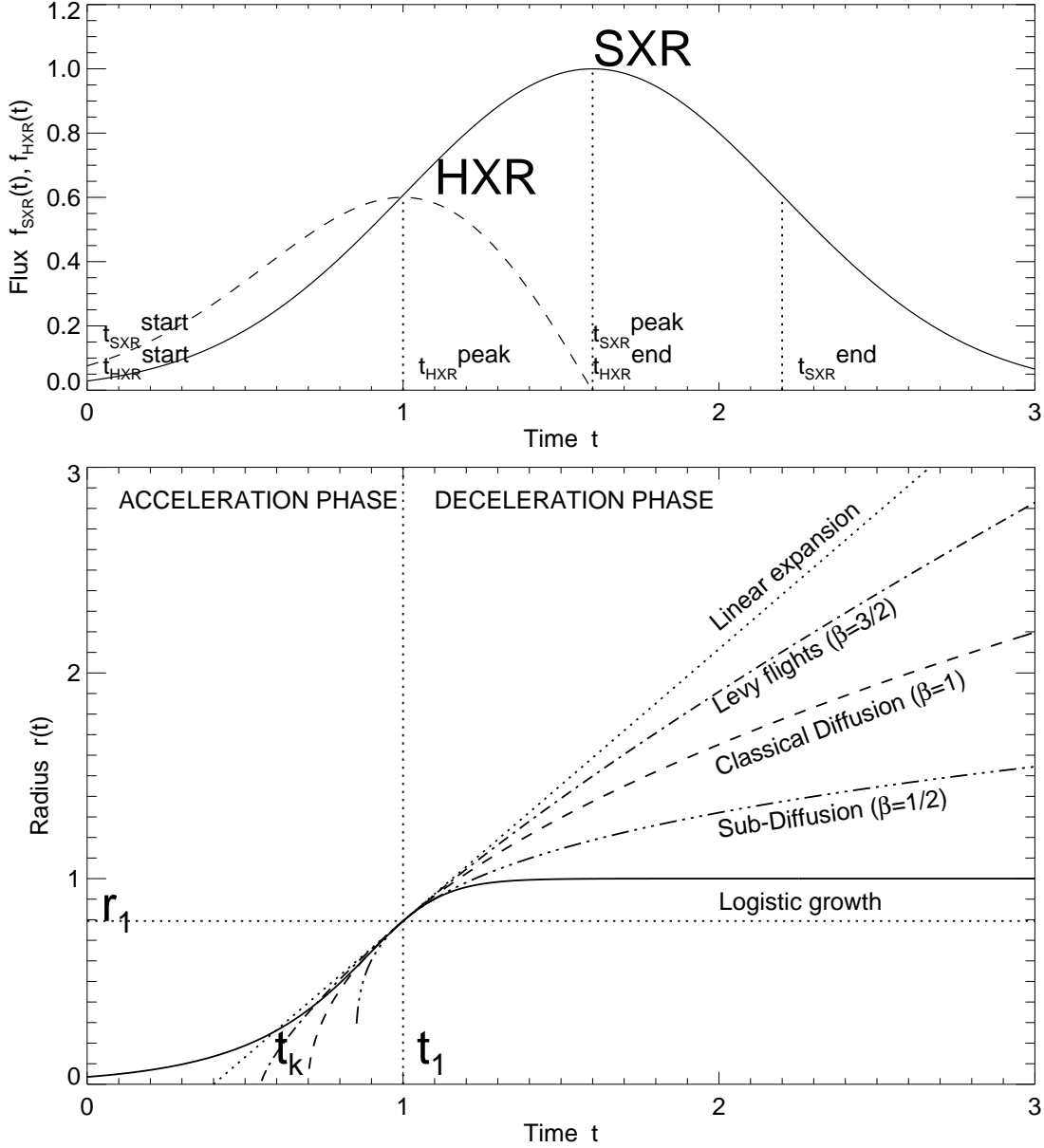


Fig. 1.— *Top*: Time evolution of the soft X-ray flux $f_{SXR}(t)$ and hard X-ray flux $f_{HXR}(t) \approx df_{SXR}/dt$ during a flare, following the Neupert effect. The rise time of the SXR flux, $t_{SXR}^{peak} - t_{SXR}^{start}$ coincides with the duration of the hard X-ray emission $T = t_{HXR}^{end} - t_{HXR}^{start} = t_{SXR}^{peak} - t_{SXR}^{start}$. *Bottom*: Comparison of spatio-temporal evolution models: Logistic growth with parameters $t_L = 1.0, r_\infty = 1.0, \tau_G = 0.1$, sub-diffusion ($\beta = 1/2$), classical diffusion ($\beta = 1$), Lévy flights or hyper-diffusion ($\beta = 3/2$), and linear expansion ($r \propto t$). All three curves intersect at $t = t_L$ and have the same speed $v = (dr/dt)$ at the intersection point at time $t = t_L$ (adapted from Aschwanden 2012b).

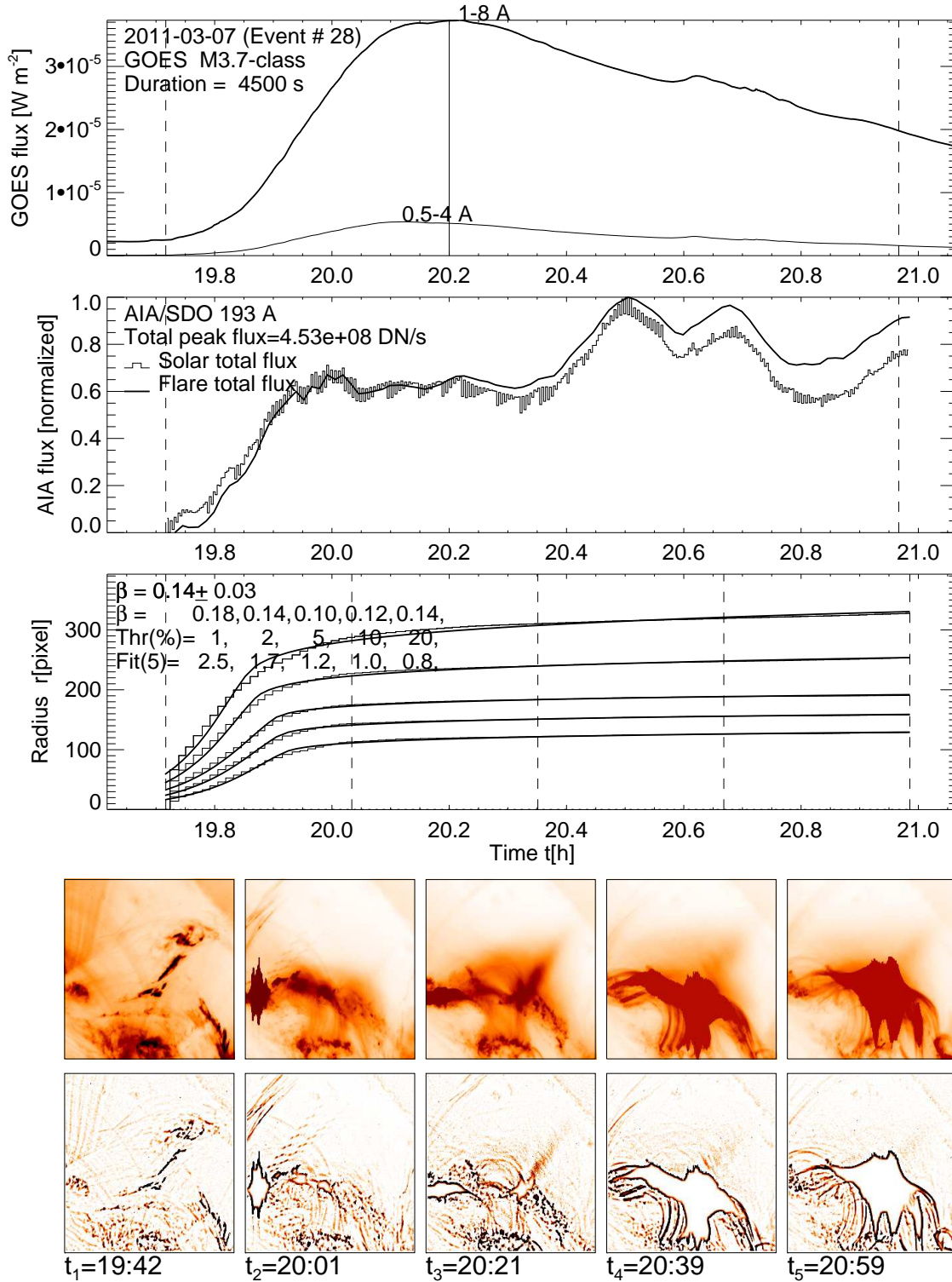


Fig. 2.— Flare event #28 was observed on 2011 March 7, 19:43-20:58 UT, with AIA/SDO 193 Å. The panels show the GOES time profiles (top panel), the total flux (second panel), the spatio-temporal evolution of the radius $r_{193,th}(t) = \sqrt{A(t)/\pi}$ of the time-integrated flare area $A(t)$ for 5 different thresholds, i.e., 1%, 2%, 5%, 10%, 20% of the peak flux (third panel: histogrammed), fitted with the anomalous diffusion model (third panel: solid curves), and five snapshots of the 193 Å flux (fourth row of panels), and highpass-filtered flux (bottom row of panels).

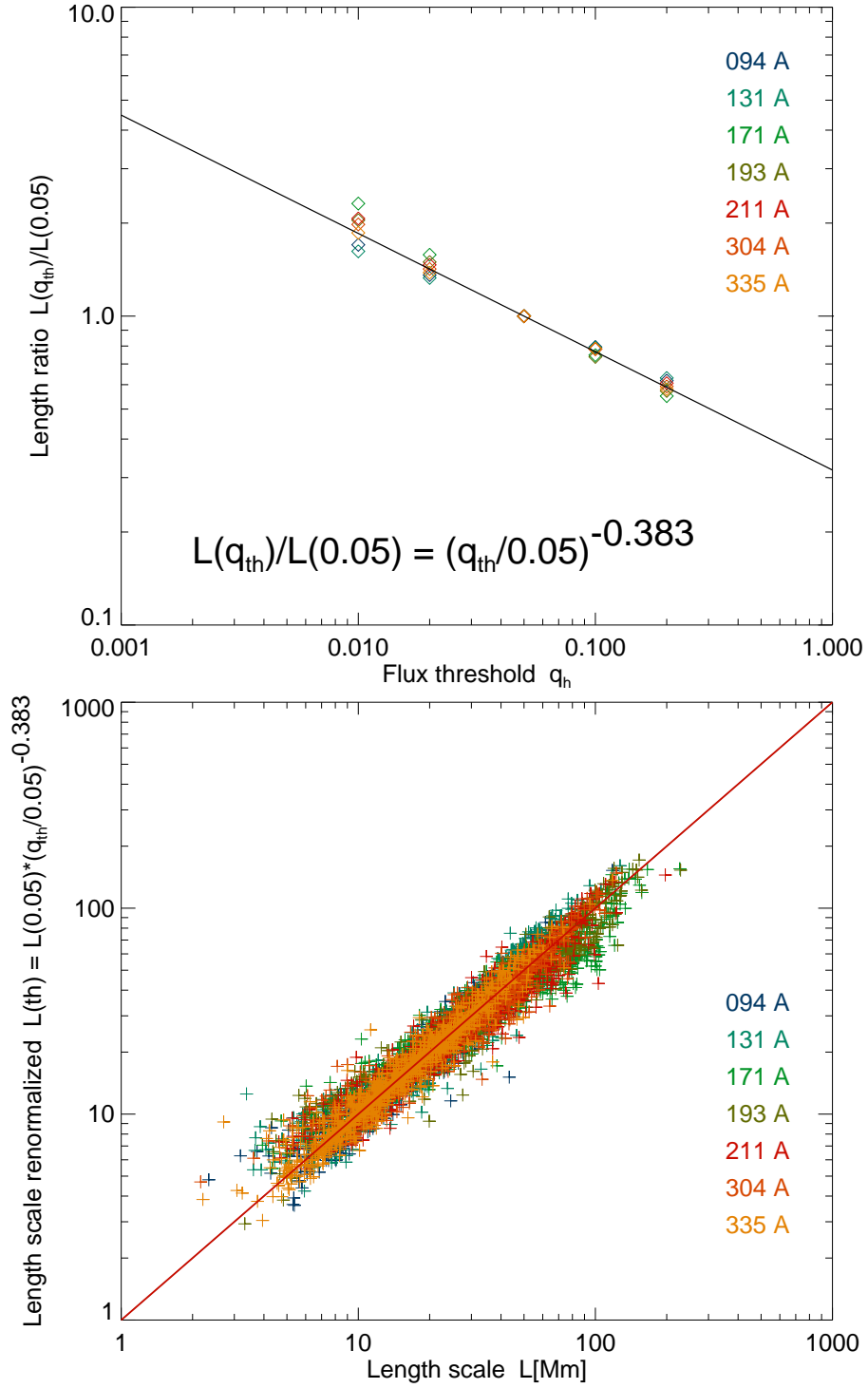


Fig. 3.— The normalization of the length scale L for different thresholds $q_{th} = 0.01, 0.02, 0.05, 0.1, 0.2$ is shown for 7 different wavelength filters (different colors). The mean ratios of the measured length scales $L(q_{th})/L(0.05)$ as a function of the threshold q_{th} is shown in the top panel, and the renormalized length scales $L_{\lambda}(q_{th}) = L_{\lambda}(0.05) \times (q_{th}/0.05)^{-0.383}$ are shown in the bottom panel for all 155 flares and 7 wavelengths (different colors).

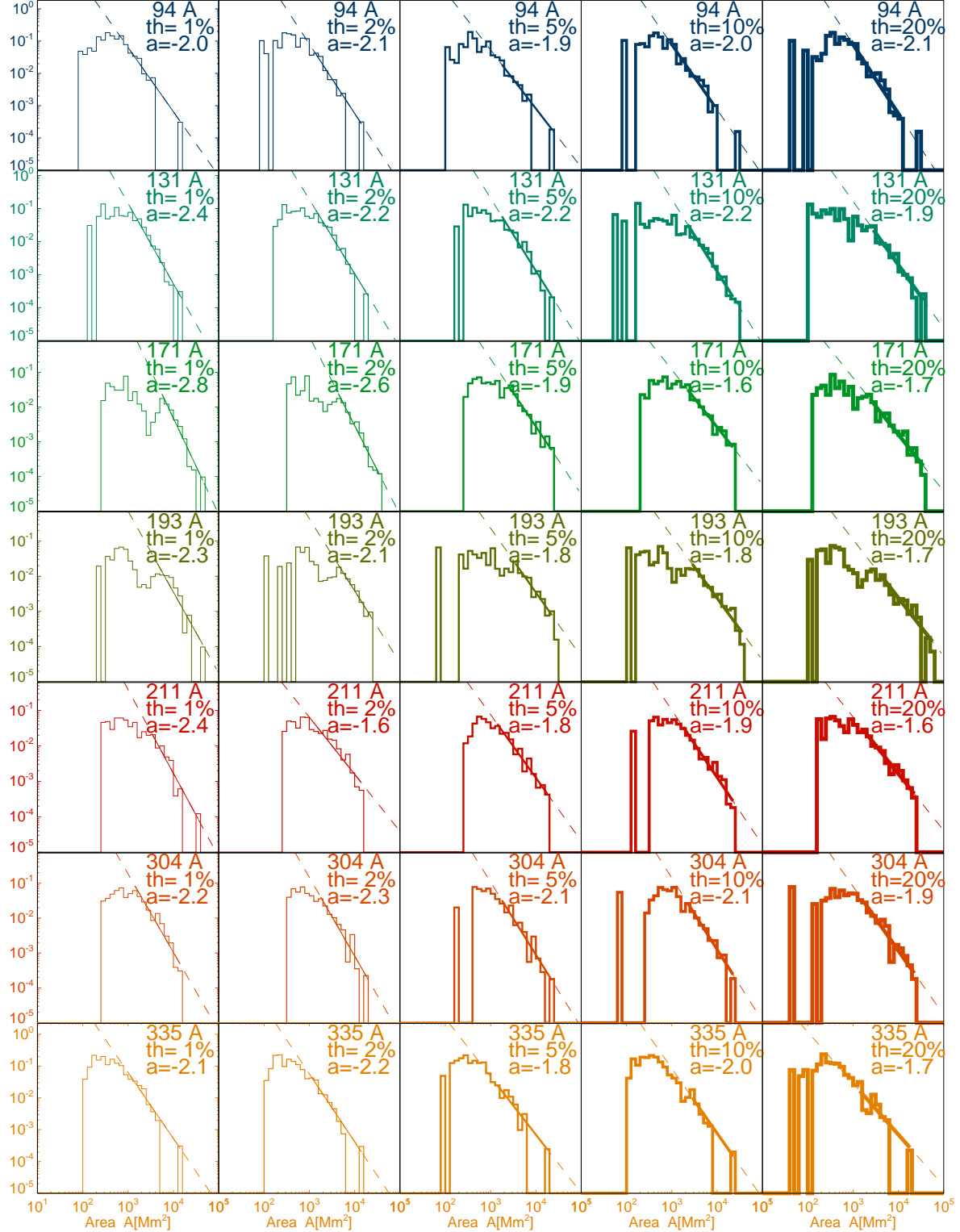


Fig. 4.— Log-log histograms $N(A)$ of measured flare areas A are shown for the dataset of 155 analyzed events, for 7 different wavelengths (rows; marked with identical color) and for 5 different flux thresholds (columns; marked with line thickness increasing as a function of the flux threshold). Powerlaw fits are obtained in the logarithmic area range of $0.05A_{max} \leq A \leq A_{max}$, with the powerlaw slopes indicated in each panel and listed in Table 2.

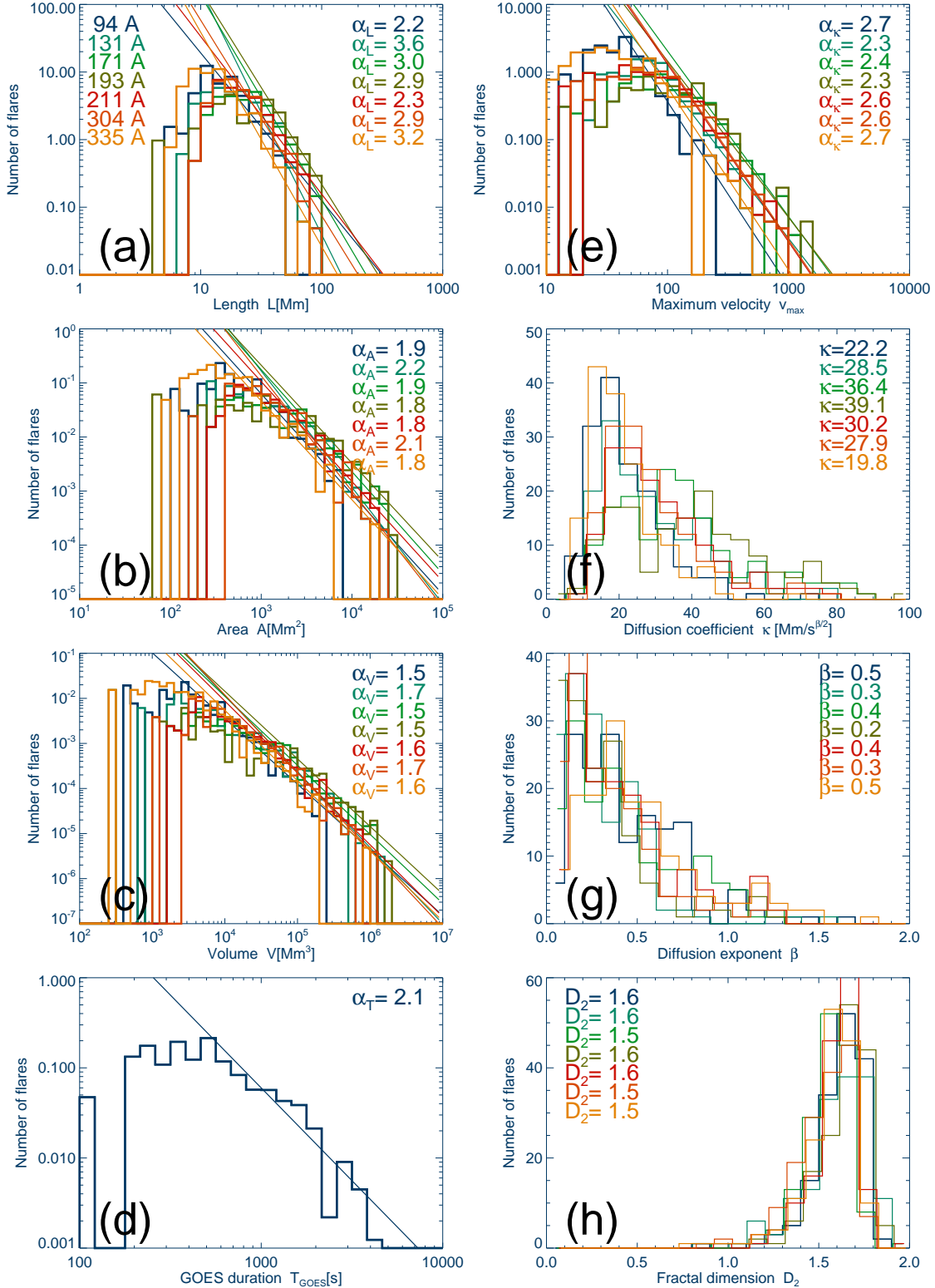


Fig. 5.— Log-log histograms of length scales l , areas A , volumes V , GOES flare durations T , diffusion coefficients κ , diffusion exponents β , maximum velocity v_{max} , and 2-D fractal dimensions D_2 sampled from the 155 analyzed flares, in each of the 7 wavelengths (94, 131, 171, 193, 211, 304, 335 Å, marked with different colors), for a threshold of $q_{th} = 5\%$. The fitted powerlaw slopes are indicated for each wavelength separately in each panel.

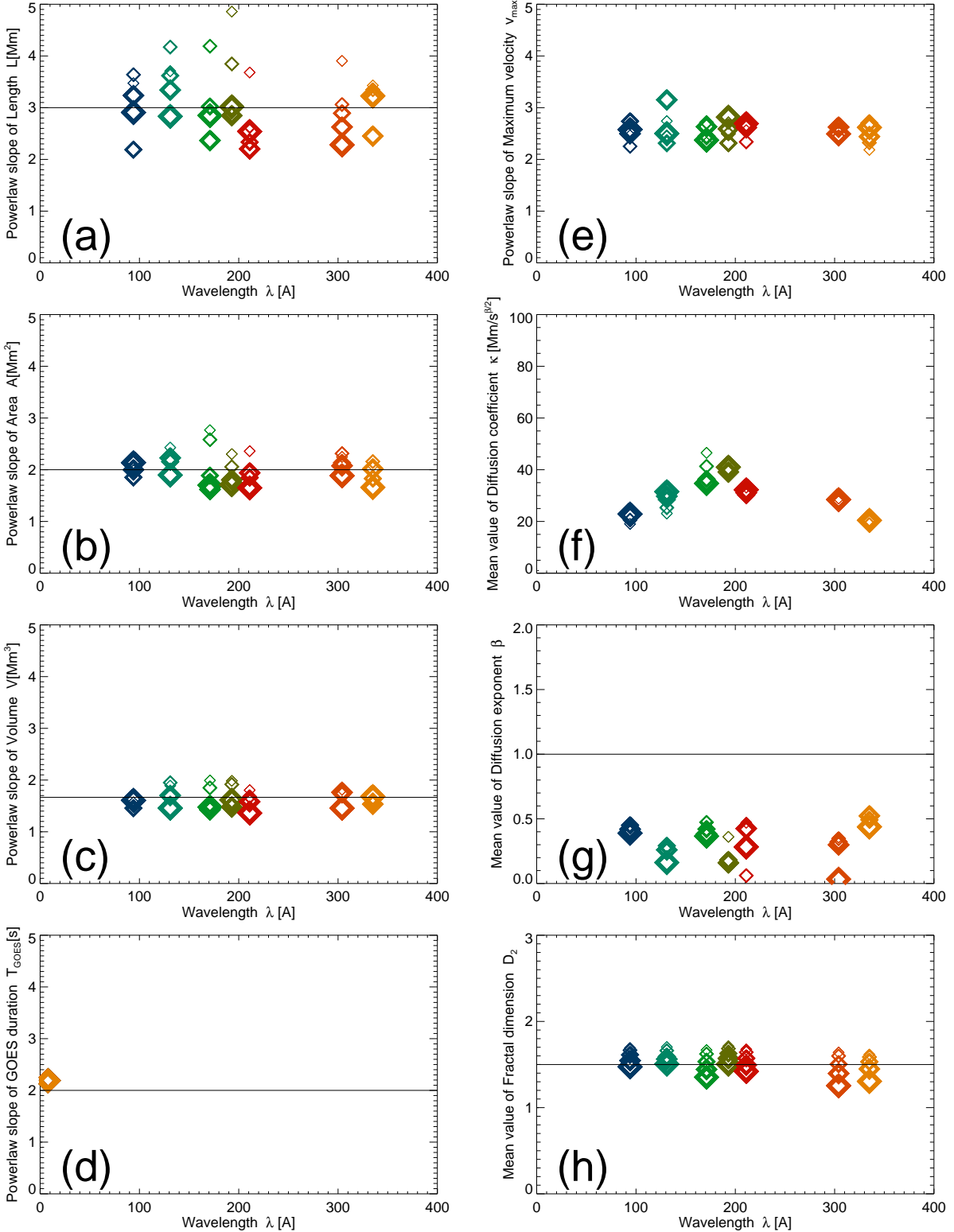


Fig. 6.— Powerlaw indices α and fractal dimension D_2 as a function of the wavelength λ (with different colors). The size of the diamond symbols indicate the t flux threshold levels. The values predicted by the FD-SOC model are indicated with a horizontal line.

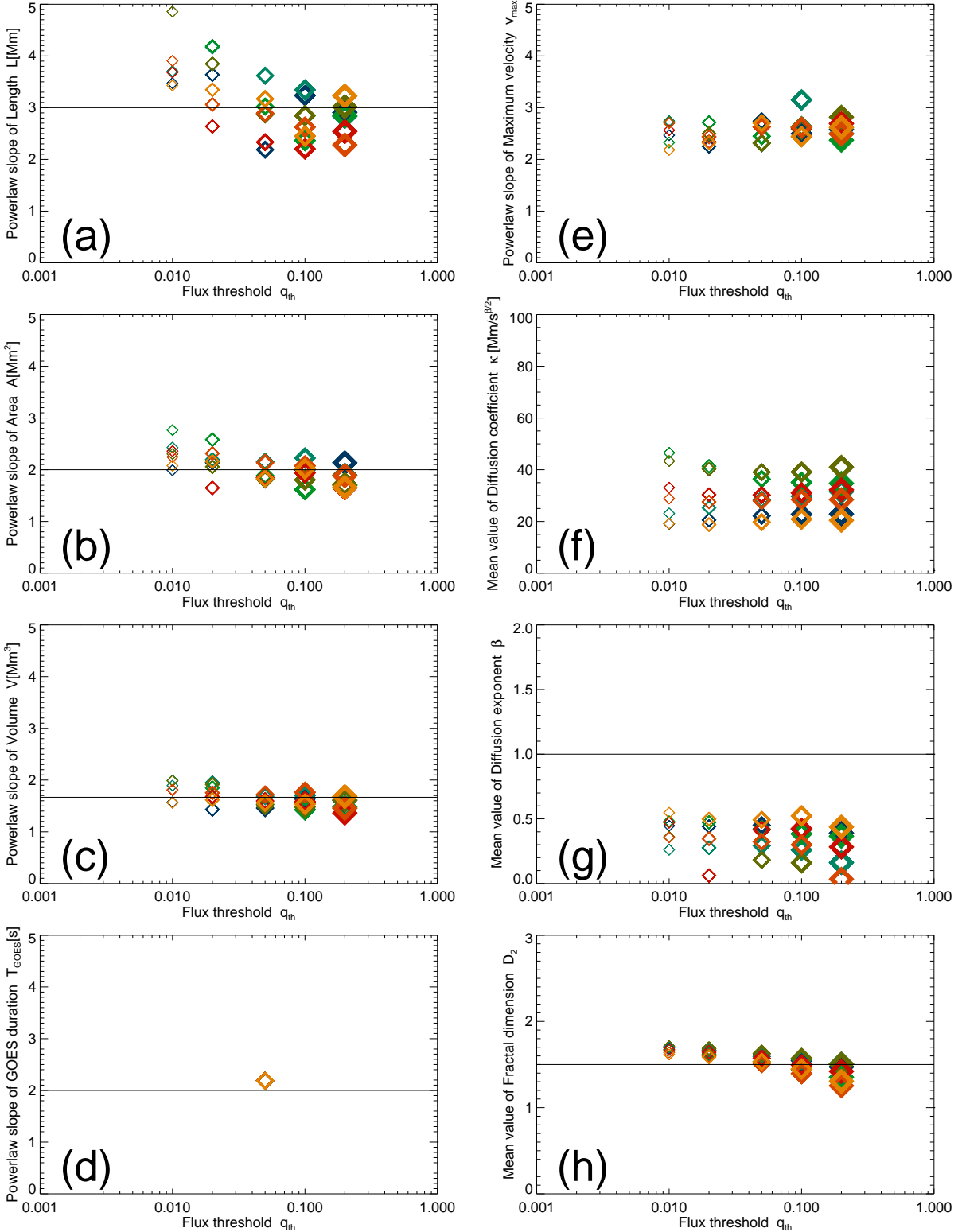


Fig. 7.— Powerlaw indices α and fractal dimension D_2 as a function of the flux threshold q_{th} (with different diamond sizes). The color indicates the wavelength. The values predicted by the FD-SOC model are indicated with a horizontal line.

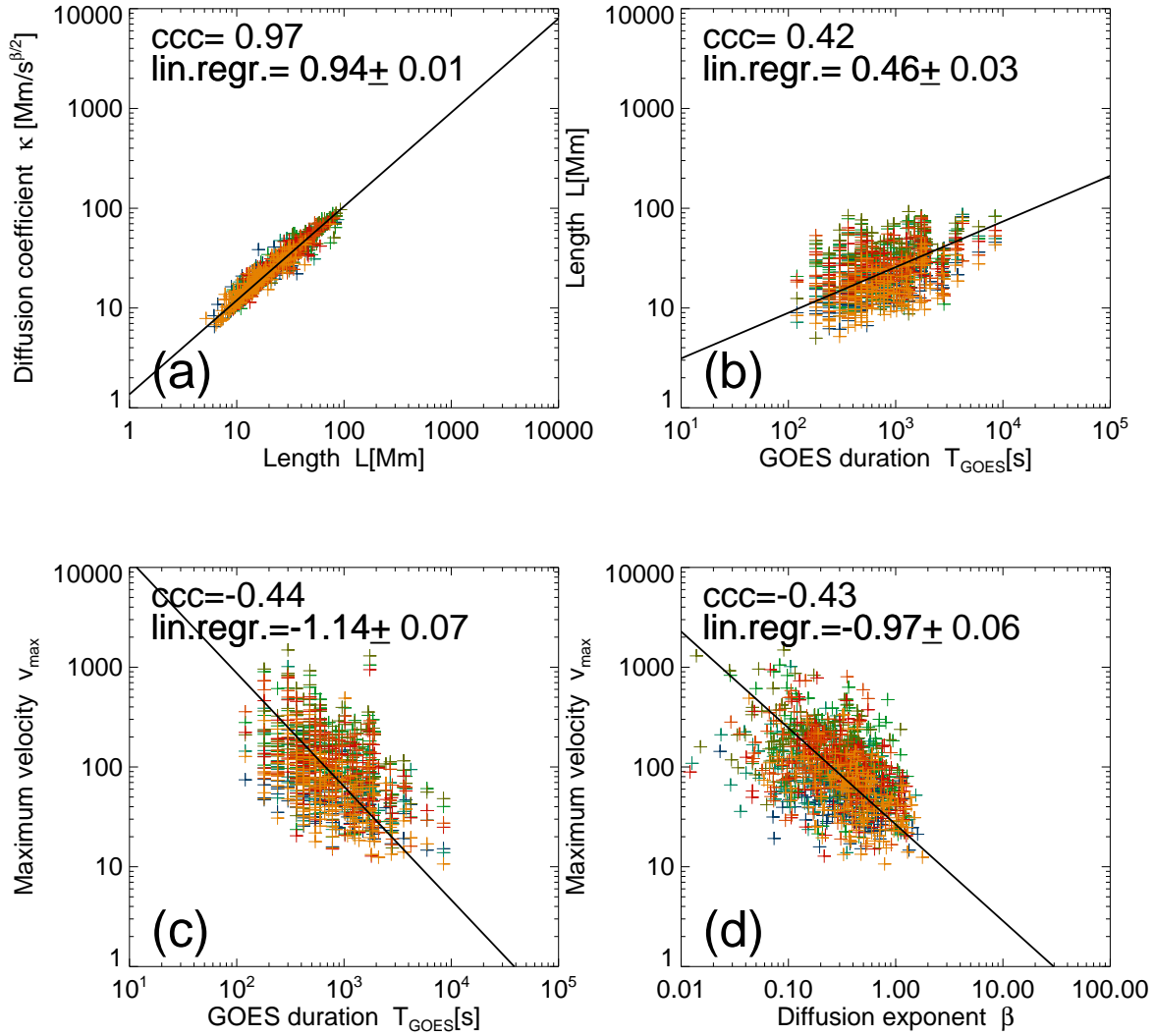


Fig. 8.— Scatterplots between correlated parameters of the length scale L , the (GOES) time duration T , the diffusion exponent β , and the maximum velocity v_{max} , for 7 different wavelengths (in different colors) using a flux threshold of $q_{th} = 5\%$. The Pearson cross-correlation coefficient (ccc) is indicated and the linear regression slope with uncertainty.

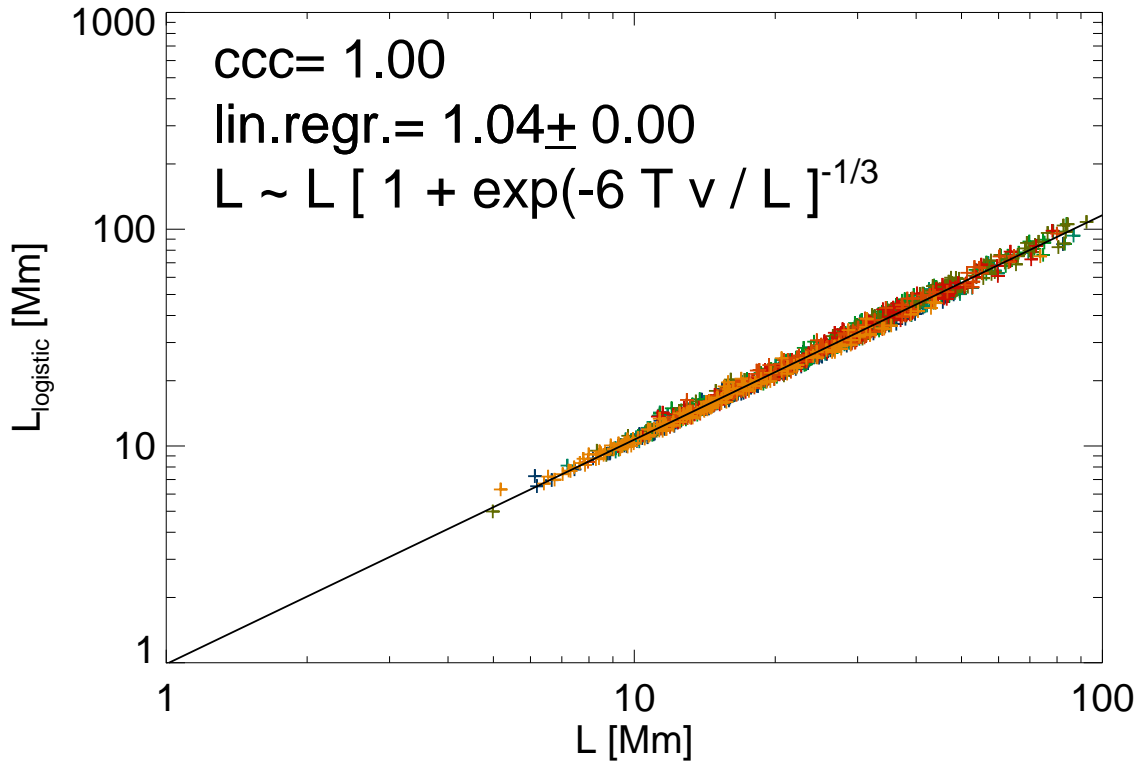
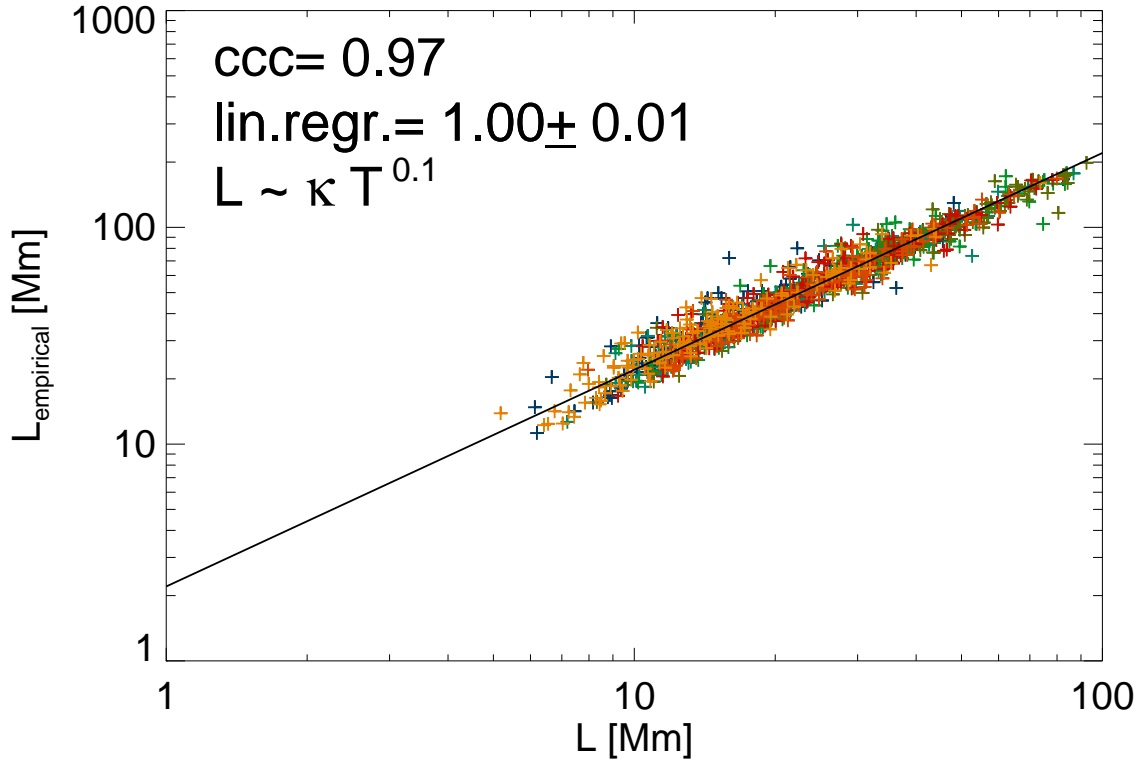


Fig. 9.— *Top*: The three-parameter correlation between the length scale L , the time scale T , and the diffusion coefficient κ shows a best fit for the relationship $L \propto \kappa T^{0.1}$, with a Pearson cross-correlation coefficient of $\text{ccc} = 0.97$.

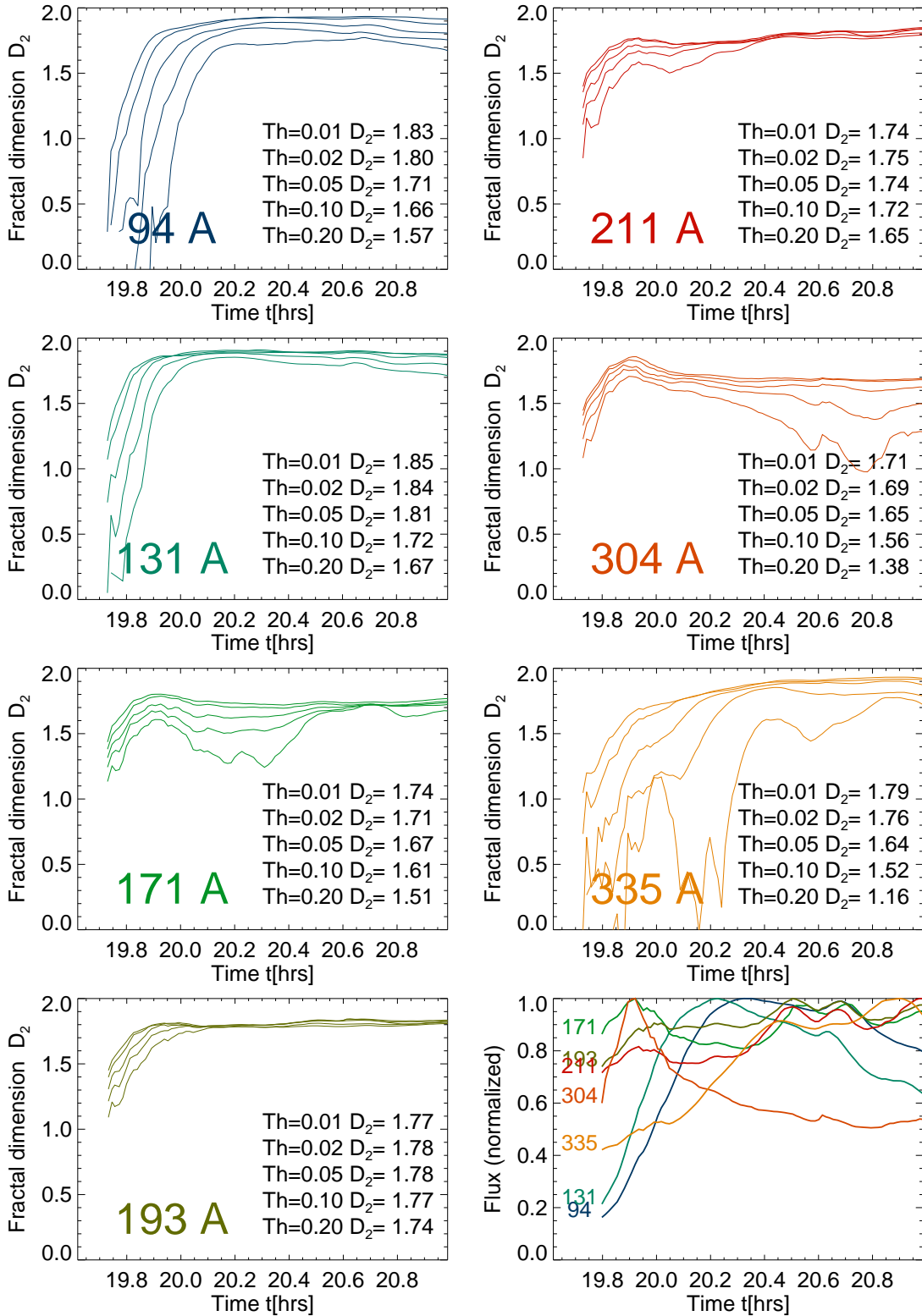


Fig. 10.— 2-D Fractal dimension $D_2(t)$ measured for events #28, 2011 March 7 (see also Fig. 2), as a function of time during the flare, shown for all 7 wavelengths (in different colors) and 5 different thresholds ($q_{th} = 1\%, 2\%, 5\%, 10\%, 20\%$). The lowest threshold yields the curve with the highest fractal dimension. For comparison, the normalized total fluxes are also shown in the bottom right panel.

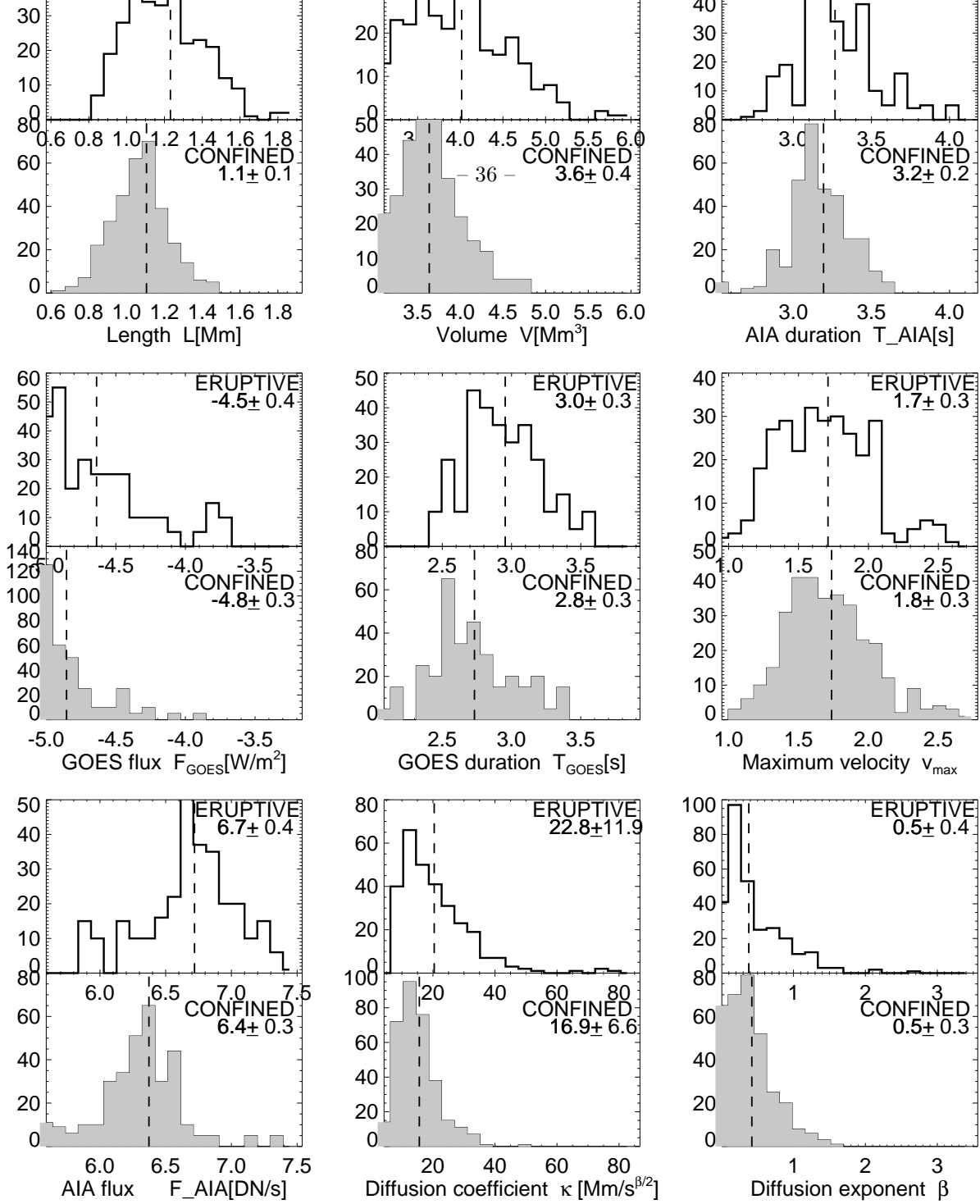


Fig. 11.— Histograms of measured flare parameters of the 155 analyzed flares (at a wavelength of 335 Å) subdivided into the two subgroups of eruptive flares (white histograms) and confined flares (grey histograms), according to the classification of Zhang and Liu (2012). The mean values and standard deviations are listed, and the mean value is marked with a vertical dashed bar.

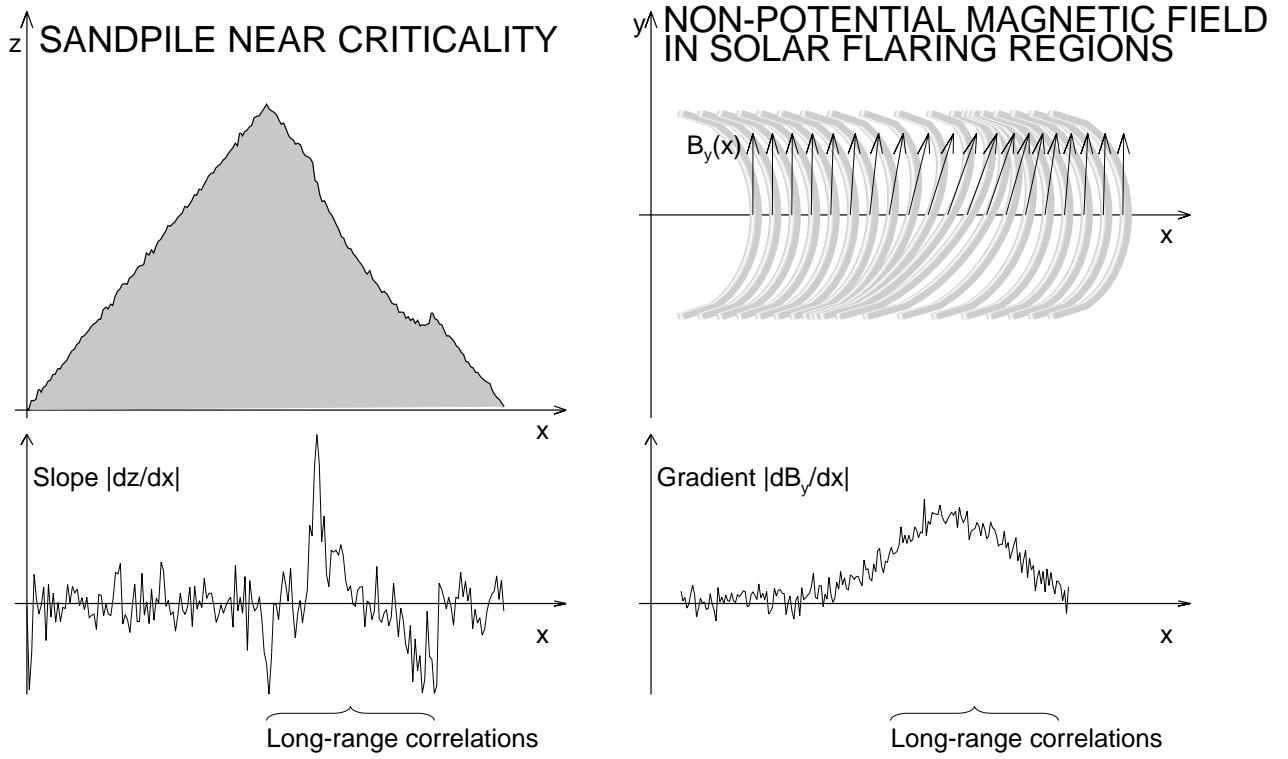


Fig. 12.— *Left:* A sandpile in a state in the vicinity of criticality is shown with a height cross-section $z(x)$, with the gradient of the slope (or repose angle) $|dz/dx|$ (bottom), exhibiting short-range fluctuations due to noise and long-range correlation lengths due to locally extended deviations from the mean critical slope. *Right:* The solar analogy of a flaring region is visualized in terms of a loop arcade over a neutral line in x -direction, consisting of loops with various shear angles that are proportional to the gradient of the field direction B_x/B_y , showing also some locally extended (non-potential) deviations from the potential field (bottom).